

IOSUD – „DUNĂREA DE JOS” UNIVERSITY OF GALAȚI

Doctoral School of Mechanical and Industrial Engineering



DOCTORAL THESIS

ABSTRACT

STUDY OF COMPLEX DIGITAL IMAGES USING STATISTICAL OPERATORS

PhD student:

Lucian Traian DIMITRIEVICI

Scientific coordinator:

Prof. Phd. Eng. Phys. Luminița MORARU

Series I4: Industrial Engineering Nr. 56.

GALAȚI

2019

IOSUD – „DUNĂREA DE JOS” UNIVERSITY OF GALAȚI

Doctoral School of Mechanical and Industrial Engineering



STUDY OF COMPLEX DIGITAL IMAGES USING STATISTICAL OPERATORS

PhD student:

Lucian Traian DIMITRIEVICI

Președinte

Scientific coordinator

Prof. PhD. Eng. Phys. Luminița MORARU

Scientific referrers

Prof. PhD. Mirela PRAISLER

Prof. PhD. Eng. Habil. Antoaneta ENE

Conf. PhD.. Emilian DĂNILĂ

Series I4: Industrial Engineering Nr. 56.

GALAȚI

2019

Seriile tezelor de doctorat susținute public în UDJG începând cu 1 octombrie 2013 sunt:

Domeniul fundamental ȘTIINȚE INGINEREȘTI

- Seria I 1: **Biotehnologii**
Seria I 2: **Calculatoare și tehnologia informației**
Seria I 3: **Inginerie electrică**
Seria I 4: **Inginerie industrială**
Seria I 5: **Ingineria materialelor**
Seria I 6: **Inginerie mecanică**
Seria I 7: **Ingineria produselor alimentare**
Seria I 8: **Ingineria sistemelor**
Seria I 9: **Inginerie și management în agricultură și dezvoltare rurală**

Domeniul fundamental ȘTIINȚE SOCIALE

- Seria E 1: **Economie**
Seria E 2: **Management**
Seria SSEF: **Știința sportului și educației fizice**

Domeniul fundamental ȘTIINȚE UMANISTE ȘI ARTE

- Seria U 1: **Filologie- Engleză**
Seria U 2: **Filologie- Română**
Seria U 3: **Istorie**
Seria U 4: **Filologie - Franceză**

Domeniul fundamental MATEMATICĂ ȘI ȘTIINȚE ALE NATURII

- Seria C: **Chimie**

Domeniul fundamental ȘTIINȚE BIOLOGICE ȘI BIOMEDICALE

- Seria M: **Medicină**

ACKNOWLEDGMENTS

The completion of my doctoral thesis, which ends an important stage of my professional training, was achieved due to quality scientific guidance conducted with professionalism and adequate conditions necessary for the research activity. This thesis is not only my work and effort, but it is also due to those who helped me and were, professionally, by my side.

I would like to thank my doctoral supervisor, prof. Luminița Moraru, for the rigorous coordination in the structuring and writing of the present endeavor and the support and encouragement received from her, during these years.

I thank the entire staff of the Faculty of Sciences and Environment of "Dunărea de Jos" University of Galați for the scientific and friendly environment created and especially my colleague, today a doctor in sciences, Ms. Simona Moldovanu for the close collaboration on the processing of information from digital images in scripts implemented in the Matlab language necessary to obtain the results of my research activity. I used a segmentation algorithm implemented by her research team that performs the removal of the respective skull, of the fatty tissue, and aligns the images, based on the hemispheric intermediate fissure.

I also wish to thank the radiologist Dr. Florina Szendrei who provided me with a database of MRI images from certain subjects who were investigated in the St. Andrew's Hospital in Galați and who accepted that their diagnoses be included in my studies, by expressing informed consent.

I thank also my colleagues from "Mihail Kogălniceanu", National College from Galati for the encouragement they have offered me, repeatedly, and to my family for the unwavering support they have given me. Last but not least, I thank God for giving me confidence in my strength, tenacity and work power, without which I would not have completed this thesis.

Table of contents		
Introduction	8	13
Motivation	8	15
The research objectives pursued	9	16
Thesis structure	10	13
Chapter I	11	20
Basic principles of magnetic resonance imaging	11	20
1.1 The role of diffusion in imaging	11	20
1.2 Diffusion of water molecule measurement in magnetic resonance imaging MRI	11	22
1.3 DTI advanced measurements and analysis	13	27
1.4 Types of MRI images	15	34
Chapter II	16	36
MRI complex images	16	36
2.1 Representation of digital images	16	36
2.2 Types of images	17	40
Chapter III	19	43
Quality enhancement of the complex digital images	19	43
3.1 Stages of the processing operations	19	43
3.2 Artifacts in digital images	19	44
3.3 Methods of improving a digital image	19	44
	20	47
3.4 Quality Descriptors	20	47
3.4.1 Mean square error	20	48
3.4.2 Peak signal-to-noise ratio	20	48
3.4.3 Normalized cross-correlation	20	48
3.4.4 Coefficient of correlation	20	48
3.4.5 Structural content	20	48
3.4.6 The average difference	21	49
Chapter IV	21	49
Anatomo-structural asymmetry and textural anisotropy of the brain		
4.1 Quality and similarity metrics used in the analysis of anatomo-structural asymmetry	21	50
	21	51
4.2 Personal contributions		
4.2.1 Assessment of the cerebral structural asymmetry assessed based on histogram analysis and similarity metrics	21	51
	21	52
4.2.1.1 Difference between histograms		
4.2.2 MRI characterization of brain structure using structural similarity and entropy	25	56
	26	56

4.2.2.1 SSIM, FSIM	26	57
4.2.2.2 Entropy		
4.2.3 Texture anisotropy methods in brain degenerative diseases investigation	31	62
4.2.3.1 Non-local means filter NLM	31	64
4.2.3.2 Co-occurrence matrix of	31	64
	31	65
4.2.3.3 Morlet Wavelet Transform	31	65
4.2.3.4 Hessian Operators	32	66
4.2.3.5 Statistical analysis		
4.2.4 Gaussian mixture models (GMM) for brain DTI texture characterization	37	74
4.2.4.1 Methodological approach	37	
4.2.4.2 The GMM algorithm with m components	37	
4.2.4.3 The k-means algorithm for clustering	37	
4.2.4.4 Euclidean weighted distance and multiple correlation	37	
4.2.4.5 Cluster validation	38	
4.2.4.6 Image acquisition and processing	38	
4.2.5 Gaussian Mixture Models Clustering using the first order structural features		
4.2.5.1 Combinations for Gaussian distributions		
4.2.5.2 Problem formalization		
4.2.5.3 First order structural features		
4.2.6 Conclusions	42	91
Chapter V	43	93
Weighted diffusion imaging and tensor diffusion imaging	43	93
5.1 The apparent diffusion coefficient (ADC) of water in brain tissue	43	93
5.2 Magnetic gradients field and their effects on the diffusion tensor		
5.3 Diffusion maps associated to several diffusion parameters in a hemisphere analysis	47	99
5.3.1 Assessing diffusion anisotropy	49	102
5.3.2 Three-phase plot representation (3P)	49	104
5.3.3 Detectability Index	49	104
5.4 Non-Gaussian diffusion MRI assessment of brain tissues	50	105
5.4.1 The method of extending the series	55	111
5.5 Conclusions	55	111
General conclusions and future research	57	115
Selective references	58	116
	59	118

Introduction

People perceive through images most information from the surrounding reality through the visual system following an interpretation of the images in the optical center of the brain. However, the human system of image acquisition and interpretation does not exhibit the performance of retaining fine details existing in images, and therefore several useful information is lost.

Medical imaging, as an important branch of the field of imaging, deals with the processing of complex digital medical images and is composed of a set of techniques for acquiring, storing, improving the clarity of the image and processing the information contained in the image, described below:

- The acquisition of the digital image is done with the help of scanners, optical microscopes, or medical imaging tools that generate the image from the acquired signal.
- The preprocessing aims to improve the image from a visual point of view, to reduce the noise generated by the acquisition instrument, to eliminate the artifacts, to manipulate the brightness and the contrast, to accentuate the edges of the image.
- Segmentation decomposes a digital image into decomposed components. Following this process, objects or regions of interest that satisfy certain uniformity criteria are extracted from the image.

In my paper I used public databases containing MRI images acquired from healthy patients or diagnosed with neurodegenerative but also private diseases, from St. Andrew's Hospital in Galați, mentioning that an agreement was signed with the investigated patients.

Image processing was performed in the advanced programming environment Matlab R2017b, and the predictive analyses in the statistical application SPSS 17.0.

Motivation

The main reason for choosing this research topic is its multidisciplinary nature, namely the possibility to apply knowledge specific to physics (transport physics, diffusion phenomenon in particular), mathematical statistics and computer science (by implementing scripts in different programming languages or using of software) in medicine.

The paper focuses on the interpretation of brain tissue images, starting with statistics published in The Royal Society Publishing that show that with the aging population, the current incidence of neurodegenerative diseases is steadily increasing worldwide. According to 1, in 2015 there were about 40 million patients diagnosed with neurodegenerative diseases (Alzheimer's, Parkinson's, Pick, Huntington, dementia, etc.) and the numbers will increase to about 135 million patients by 2050.

1 (<https://royalsociety.org/~media/about-us/international/g-science-statements/2017-may-aging-population.pdf>)

The research objectives pursued

According to the title of the doctoral thesis "**The study of complex digital images using statistical operators**" and of the scientific reports supported during the training period, I set out and achieved the following **major objectives**:

- Planning and organizing the database that will contain neuro-MRI images of healthy patients and those diagnosed with degenerative brain diseases. This objective was achieved throughout the five chapters, in which the personal contributions focused on the processing of three types of MRI images, which according to the scan parameters values are classified into: PDw (proton density), T1w weighted and T2w. The images used were provided by a series of patients diagnosed with various brain disorders (multiple hemorrhagic areas in the left temporal lobe, in remission; ischemic stroke in the background; MR appearance suggestive of left cerebral-fronto-parietal abscess; malignancy) of the brain; suggestive MRI appearance for hemorrhagic stroke in the chronic right parietal stage; demyelinating lesions in the bilateral periventricular and subcortical-supra-tensorial white matter, small cerebellar right hemisphere-hemispheric lesion; cerebral atrophy)
- Restoring images acquired using MRI scanners and avoiding the degradation of useful features due to artifacts.
- Improving the quality of these images by using filters, respectively by wavelets techniques,-
- Highlighting regions of interest (ROIs) of different sizes or entire regions such as the occipital, temporal, parietal lobes thus chosen from certain restrictions of the diffusion related to cellularity.
- Partial or total analysis of complex images by segmenting the image.
- Characterization of textures using descriptors extracted from the image histogram or descriptors of the co-occurrence matrix.
- Segmentation of complex images with modern techniques represented in this work by efficient segmentation algorithms optimized to minimum complexities.
- Testing and validating the chosen textural methods and models. In the last stage of each model from its own contributions, statistical data are analyzed and calculated by which the correlated models are verified, being provided with testing and evaluation methods.

Thesis structure

The doctoral thesis entitled "The Study of Complex Digital Images Using Statistical Operators" was organized in 5 chapters, to which the introduction, general conclusions and future directions of the study were added.

The introduction presents a description of the evolution of medical imaging, as a branch of the field of imaging, and lists the operations for processing, preprocessing and segmentation of images acquired from MRI scanners.

Chapter 1 describes the basic principles of magnetic resonance imaging, how to measure the water molecule diffusion in MRI magnetic resonance imaging, describes advanced DTI measurements and analyzes and finally lists the types of NMR images.

Chapter 2 presents the complex MRI images, their mathematical representation, their classification according to accuracy, and lists the types of images used in the thesis.

Chapter 3, entitled "Improvement of complex digital images", describes the steps of the processing operation, the disturbing elements in the digital images as well as the methods for improving the digital images, defining a series of quality descriptors.

Chapter 4, called "Anatomical-structural asymmetry and textural anisotropy of the brain" defines theoretical notions such as quality and similarity metrics, histogram difference, entropy, SSIM and FSIM indices, non-local filter means NLM, CM co-occurrence matrix, wavelet Morlet WM, Hessian operators. The chapter is supplemented by personal contributions in the study of structural asymmetry based on histogram analysis and similarity metrics, Characterization of brain structures from MRI images based on similarity studies and entropy, methods of investigating textural anisotropy in degenerative brain diseases, pattern mixing Gaussian (GMM) for characterizing the texture of cerebral DTI images.

Chapter 5, focused on weighted diffusion imaging and tensor diffusion imaging, describes notions such as diffusion anisotropy measures, three-phase graphical representation (3P), detectability index, extension method of the series and is supplemented by personal contributions in studies on the coefficient of diffusion. apparent diffusion of water into brain tissues, magnetic field gradients, diffusion maps, and parameters associated with the diffusion tensor as well as non-Gaussian diffusion into brain tissues.

Finally, the conclusions of the paper and future research directions are presented.

Chapter I

Basic principles of magnetic resonance imaging

1.1 The role of diffusion in imaging

Magnetic resonance imaging is a non-invasive medical imaging technique that uses strong magnetic fields and magnetic field gradients to reconstruct images of the human body. MRI data are usually acquired using echo planar imaging (EPI) technology, which uses pulse sequences to generate an imaging cycle consisting of the excitation sequence and the relaxation sequence. One of the types of NMR sequences is the one called Spin-Echo, based on a spin-echo sequence of gradient impulses.

By using magnetic pulses with certain well-established frequencies (Larmor frequency, resonance frequency), the orientation of the spines can be influenced and modified (figure 1.1). All these differences detected in the orientation or phase of the spines of the component particles of the tissues, allow the reconstruction in NMR images of the human body.

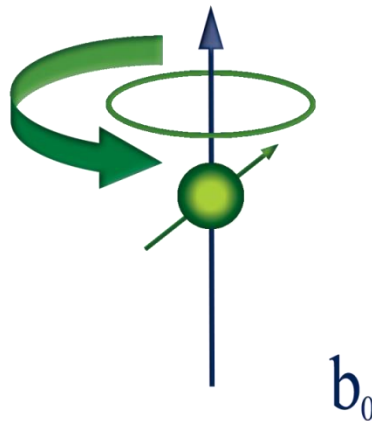


Figure 1.1. Interaction proton-magnetic field b_0

1.2 Diffusion of water molecule measurement in magnetic resonance imaging MRI

DTI is one of many magnetic resonance imaging (MRI) imaging procedures for signal detection. Within the DTI, the intensity of the measured NMR signal depends on the distance and the direction of movement of the water molecule in an image volume element (called voxel), in a manner directed by the stored thermal energy, which was initially described by Brown [1]. Thus, in the "Brownian motion", a water molecule moves in a certain environment to a certain point, at a time and at a random speed, unless the movement is limited by the barriers present in the tissues (Figure 1.2).

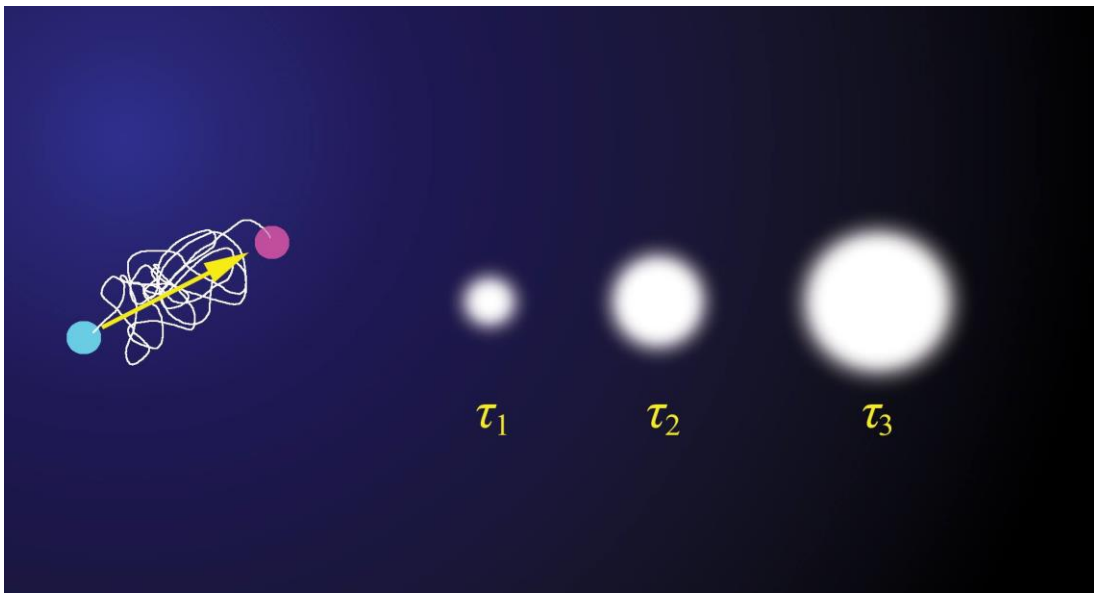


Figure 1.2 Brownian motion of a water molecule. The net displacement is from the blue point to the red point. In the case of small diffusion times (τ_1), $\tau_1 < \tau_2 < \tau_3$, the diffusion volume is compact. The diffusion volume increases with the increase of the diffusion times (τ_3)

The DTI uses a "spin-echo" pulse sequence for signal detection, described in Figure 1.3 [2]. The spin-echo sequence has a waiting time $TE / 2$. The following spin-echo sequence produces a second electromagnetic impulse at the $TE / 2$ moment and has the effect of reversing the loss of coherence between signals that occurred during the $TE / 2$ period.

Signal detection

Diffusion Sensitizing gradient

Radiofrequency transmitter

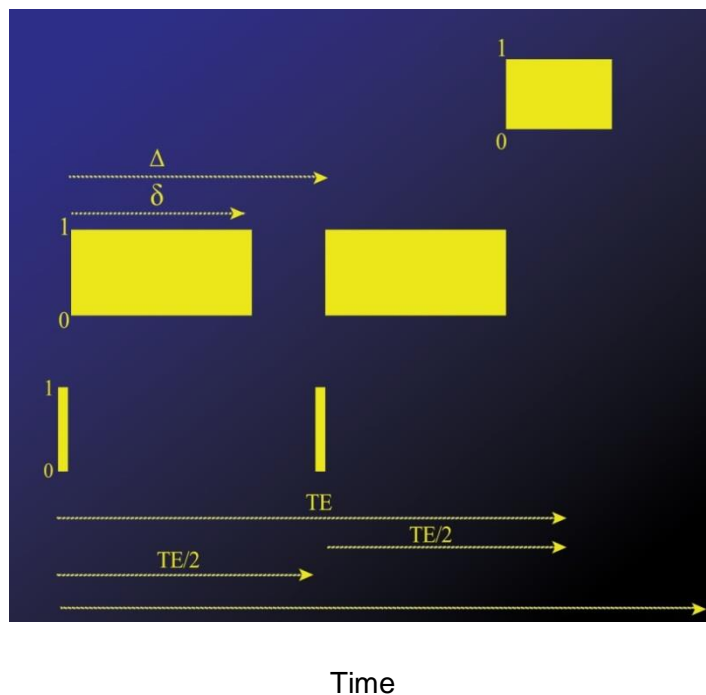


Figure 1.3 Key elements of the spin-echo pulse sequence used for DTI. The timing of off-on (0/1) events for the three most important MRI scanner subsystems (Radiofrequency transmitter Diffusion Sensitizing Gradient and signal detection).

1.3 DTI advanced measurements and analysis

In the mature human brain, white matter WM is the one that produces easily measurable directional effects. A conceptual diagram illustrating DTI's DTI principles is shown in Figure 1.4. The colored lines in this figure simulate the random movements of a group of water molecules while moving from the same point in space. In WM, the most important internal barriers are the axonal membranes. Figure 1.4 shows how the WM diffusion coefficient parallel to the axonal matrix is equal to the GM diffusion coefficient measured in either direction.

The diffusion in CSF and GM structures is isotropic and in WM anisotropic. However, there are studies that report conflicting results, especially when tissues containing non-myelinated young axons have been studied.

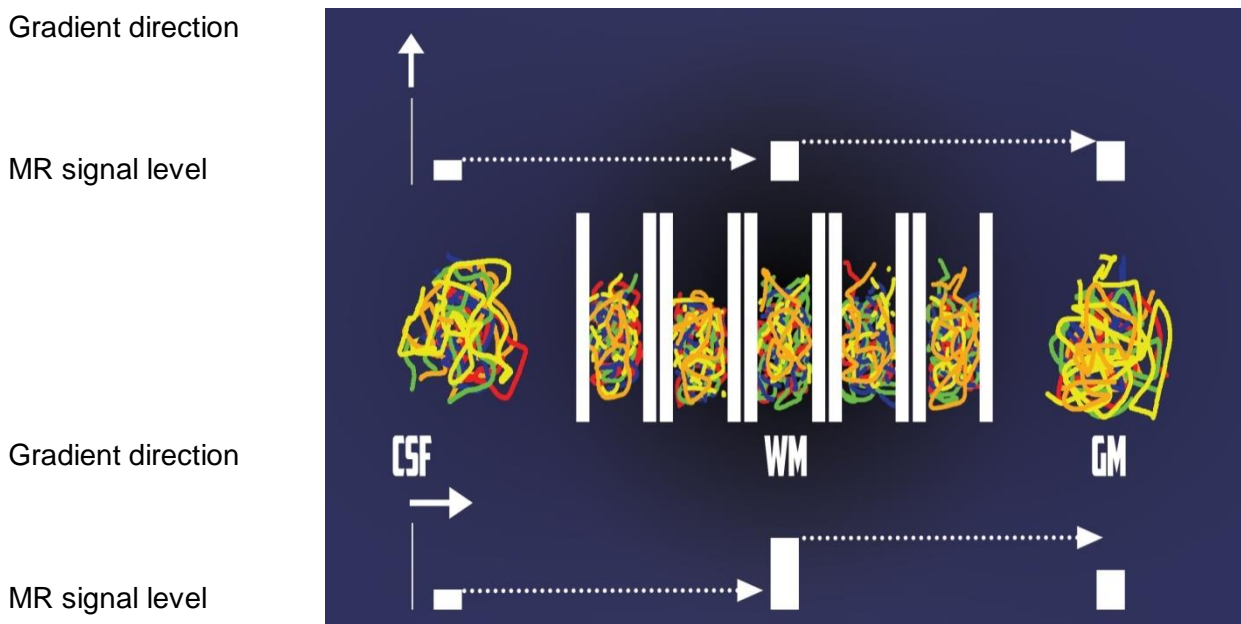


Figure 1.4 DTI concept diagram. The middle panel illustrates water molecule diffusion trajectories in CSF, white matter and gray matter. The top and bottom panel illustrate the effect of gradient sensitizing direction on MRI signal intensity from these tissue regions.

A complete spatial encoding of the signal of the magnetic field gradient on the three orthogonal axes Ox, Oy, Oz of the diffusion tensor D is expressed as follows:

$$D = \begin{bmatrix} D_{xx} & D_{xy} & D_{xz} \\ D_{yx} & D_{yy} & D_{yz} \\ D_{zx} & D_{zy} & D_{zz} \end{bmatrix} \tag{1.1}$$

D is usually assumed to be a diagonally symmetric matrix ($D_{ij}=D_{ji}$, $i,j=1,3$) and therefore only 6 of the 9 elements are unique. If the values of the 6 tensor terms are known, it is possible to calculate the value of the diffusion coefficient in any arbitrary direction in space.

$$D = \begin{bmatrix} D_{xx} & D_{xy} & D_{xz} \\ D_{xy} & D_{yy} & D_{yz} \\ D_{xz} & D_{yz} & D_{zz} \end{bmatrix} \quad (1.2)$$

The eigenvalues are just the directionally specific Einstein-Smoluchowski diffusion coefficient in the direction specified by their corresponding eigenvector. The eigenvalues are usually given the symbol λ and are usually referred to as $\lambda_1, \lambda_2, \lambda_3$, with λ_1 being the principal eigenvalue which is larger than λ_2 and λ_3 . For WM it is sometimes assumed that λ_2 equals λ_3 and the diffusion is said to display 'axial symmetry'. Images that convey the value of the diffusion coefficients (equivalent to the eigenvalues) are sometimes presented in DTI studies. These may be images of λ_1, λ_2 and λ_3 or images of Mean Diffusivity (MD):

$$MD = \frac{1}{3}(\lambda_1 + \lambda_2 + \lambda_3) \quad (1.3)$$

The Axial Diffusivity (AD) or $D_{||}$ is:

$$AD = \lambda_1 \quad (1.4)$$

Radial Diffusivity (RD) or D_{\perp} is:

$$RD = \frac{1}{2}(\lambda_2 + \lambda_3) \quad (1.5)$$

These last two sizes are not independent of MD, because:

$$MD = \frac{D_{||} + 2D_{\perp}}{3} \quad (1.6)$$

In some cases $Tr(D)$ is used instead of MD because the trace of the diffusion tensor is equivalent to the sum of the eigenvalues. This is a measure of the diffusion size and is invariable by rotation.

$$Tr(D) = \lambda_1 + \lambda_2 + \lambda_3 \quad (1.7)$$

In addition to λ_1 , λ_2 , λ_3 , MD and RD, a simple summary image can be formed of the 'Fractional Anisotropy' (FA) (Basser et al. [18]).

$$FA = \sqrt{\frac{(\lambda_1 - \lambda_2)^2 + (\lambda_1 - \lambda_3)^2 + (\lambda_3 - \lambda_2)^2}{2(\lambda_1^2 + \lambda_2^2 + \lambda_3^2)}} \quad (1.8)$$

Another size independent of the existence of a gradient is the apparent diffusion coefficient (ADC), which is the average of the diffusion coefficients measured in the x, y and z directions, specific to the RMN scanner. ADC characterizes water diffusion at the cellular level, using the proportionality of the signal intensity and the diffusion coefficient, and collects information on the cellularity of the tissues and the integrity of the cell membranes.

It is also possible to form a colorized image that helps to convey the direction of the principal eigenvector (Pajevic et al. [42]).

Figure 1.5 provides one such example in the DTI called "ColorMap", (CM) in which the red-green-blue color system shows the directions of its own vectors.

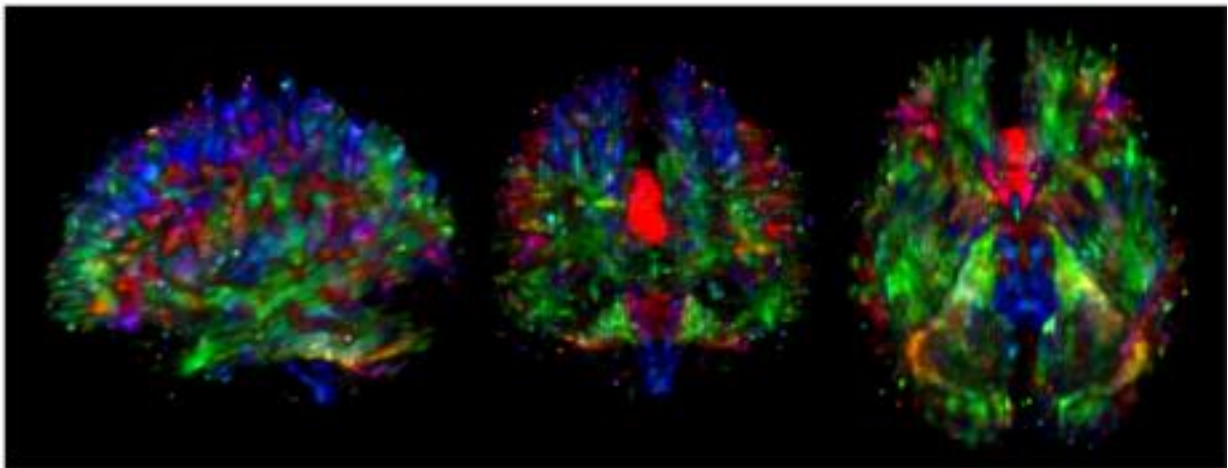


Figure 1.5 Three-dimensional volume renderings of DTI CM. Left lateral, frontal and cranial views are provided. The red color indicates the left-right direction, the anterior-posterior green direction and the upper-inferior blue color.

1.4 MRI image types

Depending on the scan parameters (for example TR = repetition time, TE = echo time), the values are classified into:

- PDw (TR long / TE short)
- weighted T1w (TR short / TE short)
- weighted T2w (TR long / TE long)

Chapter II

MRI complex images

Digital images are an artificial representation of real images. Castleman et al. [4] classify the images, according to the acquisition principle, as follows:

- abstract images, obtained by mathematical modeling;
- visible images, obtained by photography techniques;
- non-visible images, obtained by X-ray, ultrasound, magnetic or nuclear resonance, etc.

2.1 Representation of digital images

The images represent two-dimensional signals that reflect the gray level in the point of coordinates x and y . A two-dimensional image can be expressed as a continuous or discrete pattern [5]. Temporal discretization is called sampling and discretization in amplitude is called quantization. By sampling and quantization, the transition from continuous to the discrete domain is realized:

1) Sampling is defined as retrieving the intensity and color informations from the image in points on a sampling grid [6]:

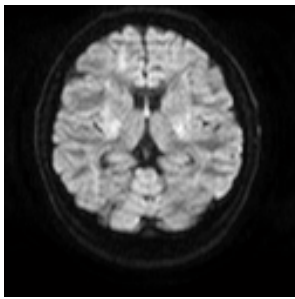
$$f(x,y) = \begin{pmatrix} f(0,0) & f(0,1) & \dots & f(0,M-1) \\ f(1,0) & f(1,1) & \dots & f(1,M-1) \\ \vdots & \vdots & \ddots & \vdots \\ f(N-1,0) & f(N-1,1) & \dots & f(N-1,M-1) \end{pmatrix} \quad (2.1)$$

2) Quantisation is a process of transforming the value of a function $f(x,y)$ into discrete values.

Digital images are made up of image elements called pixels. The types of images used in this study are:

- binary images, (figure 2.2) are represented by a logical array where each pixel is represented on one bit;
- in the grayscale images (figure 2.1) the pixel values are the result of the illumination intensity [7, 8].
- RGB images (figure 2.3), where each pixel is represented by three values in RGB space with values between $[0, 65535]$ or $[0,1]$ (figure 2.4).
- in the indexed images the value of each pixel is an index which encodes the color of that pixel.
- 3D digital images or volumetric images (Figure 2.5) are obtained from a series of 2D digital images, in a series of parallel planes.

MRI complex images



	40	41	42	43	44	45	46	47	48	49	50
53	109	108	123	133	117	109	129	148	146	137	138
54	134	129	104	124	130	115	132	153	147	144	151
55	138	133	71	86	143	147	142	156	155	156	165
56	118	127	83	54	118	151	151	154	156	161	171
57	100	118	109	84	66	105	149	154	146	158	173
58	102	108	114	122	86	65	130	153	140	156	169
59	110	108	116	130	127	107	112	140	148	154	156
60	113	117	121	114	125	128	114	129	156	150	147
61	106	112	108	98	97	106	117	129	143	135	129

Figure 2.1 Representation of a grayscale image.



	44	45	46	47	48	49	50	51	52	53	54
89	1	1	1	1	1	0	1	1	1	1	1
90	1	1	1	1	1	0	1	0	0	1	1
91	1	1	1	1	0	1	1	0	0	1	1
92	1	1	1	0	0	1	1	0	0	1	1
93	1	1	1	1	1	1	0	0	1	1	1
94	0	0	1	1	1	1	0	1	1	1	1
95	0	0	0	0	1	0	0	1	1	1	1
96	0	0	0	0	1	0	0	1	1	1	1
97	0	0	0	0	1	0	1	1	1	1	1
98	0	0	0	0	0	0	1	1	1	1	1

Figure 2.2 Representation of a binary image.

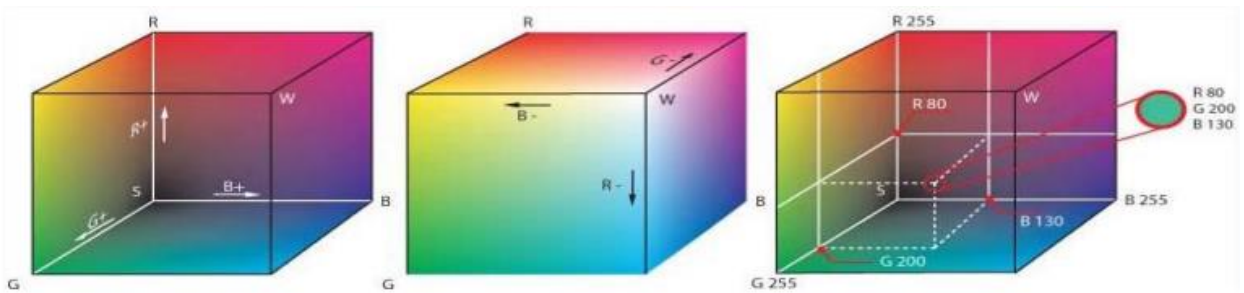
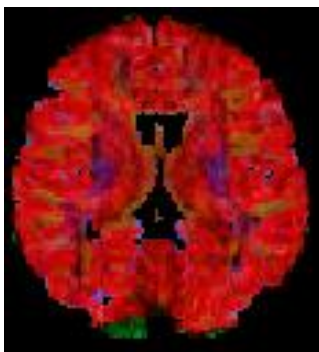


Figure 2.3 RGB color image representation.



256x256x3 double

0.6849	0.7115	0.7417	0.7528	0.7697	0.8035
0.6737	0.8192	0.8022	0.8196	0.8675	0.7998
0.6193	0.7056	0.8392	0.7951	0.7618	0.7668
0.6209	0.6163	0.6987	0.6518	0.7594	0.7743
0.6714	0.6316	0.7120	0.5984	0.7564	0.7752
0.6897	0.7448	0.7174	0.6549	0.7006	0.6271
0.6633	0.6069	0.5969	0.5747	0.6638	0.6893
0.7668	0.5725	0.5928	0.6179	0.6232	0.6481

Figure 2.4 Representation of a "double" color image.

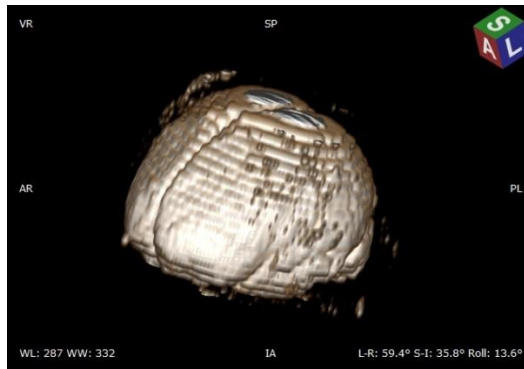


Figure 2.5 3D digital image of the brain

2.2 Types of images

In the research activity of my doctoral thesis I analyzed types of images such as: joint photographic experts group (.jpeg, .jpg), tagged image file format (.tif, .tiff), portable network graphics (.png), windows bitmap (bmp), Graphic Interchange Format (.GIF) as well as complex images such as Digital Imaging and Communications in Medicine (.DICOM) and the Neuroimaging Informatics Technology Initiative (.NifTi).

DICOM images are commonly used as a standard for data communication in medicine. They store a range of information about the patient, about the acquisition device, pixel / voxel size, gray level values, etc. as in figure 2.6.

[-E]	PatientName	1x1 struct
abc	PatientID	''
abc	PatientBirthDate	''
abc	PatientSex	''
abc	SecondaryCaptureDeviceManufa...	'MathWorks'
abc	SecondaryCaptureDeviceManufa...	'MATLAB'
abc	StudyInstanceUID	'1.3.6.1.4.1.9590.100.1.2.356534155612416426936464687822156141957'
abc	SeriesInstanceUID	'1.3.6.1.4.1.9590.100.1.2.286257452212267215805701482442548205313'
abc	StudyID	''
[+]	SeriesNumber	[]
[+]	InstanceNumber	[]
abc	PatientOrientation	''
[+]	SamplesPerPixel	1
abc	PhotometricInterpretation	'MONOCHROME2'
[+]	Rows	128
[+]	Columns	128
[+]	BitsAllocated	16
[+]	BitsStored	16
[+]	HighBit	15
[+]	PixelRepresentation	0
[+]	SmallestImagePixelValue	0
[+]	LargestImagePixelValue	183

Figure 2.6 Information provided by a DICOM image.

There are two components in a DICOM image, the first is the image and the second is the header (figure 2.6).

Chapter III

Quality enhancement of the complex digital images

3.1 Stages of the processing operations:

- acquisition of digital images
- pre-processing
- the image texture analysis
- the segmentation
- the description, recognition, classification and selection of the objects properties

3.2 Artifacts in digital images

The acquired images are, in most cases, affected by noise. Noise can also occur as a result of image transmission and compression errors and its elimination is necessary before the images are analyzed.[6, 10].

3.3 Methods of improving a digital image

- additive noise is mathematically described by the relation [11-13]:

$$g(x,y) = f(x,y) + \eta(x,y) \quad (3.1)$$

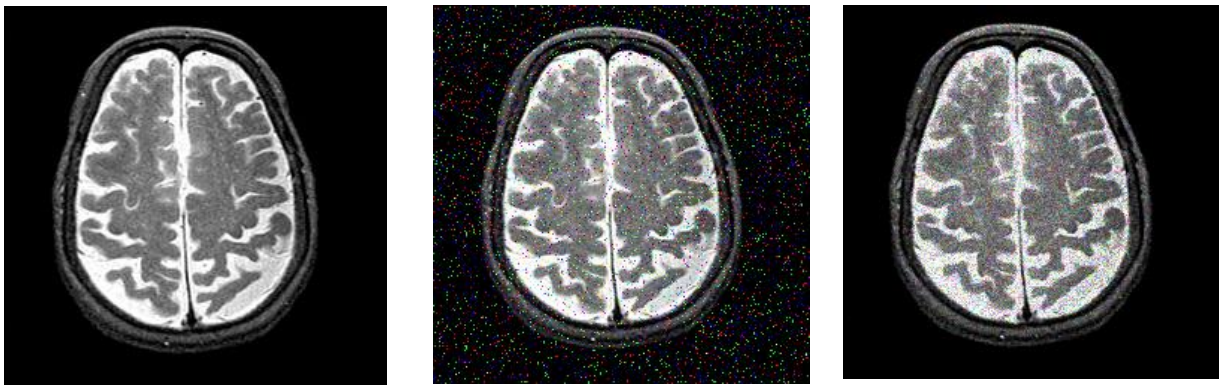
- multiplicative noise is described by:

$$g(x,y) = f(x,y) * \eta(x,y) \quad (3.2)$$

where $f(x,y)$ it's the original image, $\eta(x,y)$ is the noise and $g(x,y)$ is the image affected by noise.

- "salt and pepper" type noise. [12]

Figure 3.1 shows the effect of different types of noise on a DICOM image.



(a) The original image

(b) Image with salt and pepper noise

(c) Image with impulse noise

Figure 3.1

3.4 Quality descriptors

Segmentation performance and image quality are performed with metrics expressed by: mean square error (MSE), peak signal-to-noise ratio (PSNR), correlation coefficient (CoC), signal-to-noise ratio (SNR), structural content (SC) contrast-noise ratio (CNR) and average Difference (AD),

3.4.1 Mean square error: MSE is used to evaluate an image affected by noise, as a whole, $g(i, j)$ compared to the original image, $f(i, j)$:

$$MSE = \frac{1}{N \cdot M} \sum_{i=0}^{N-1} \sum_{j=0}^{M-1} (g(i, j) - f(i, j))^2 \quad (3.6)$$

3.4.2 Peak signal-to-noise ratio: PSNR consider only the maximum possible value of the signal in the initial image $f(i, j)$, without further evaluating the signal variation in that image:

$$PSNR = 10 \log \frac{N \cdot M \left(\max_{i,j} f(i, j) \right)^2}{\sum_{i=0}^{N-1} \sum_{j=0}^{M-1} (g(i, j) - f(i, j))^2} \quad (\text{dB}) \quad (3.7)$$

3.4.3 Normalized cross-correlation: NCC offers the proximity between two digital images ensuring the degree of similarity or proximity between two images:

$$NCC = \frac{1}{N \cdot M} \frac{\sum_{i=0}^{N-1} \sum_{j=0}^{M-1} (g(i, j) - \bar{g}(i, j)) [f(i, j) - \bar{f}(i, j)]}{\sqrt{\sum_{i=0}^{N-1} \sum_{j=0}^{M-1} [g(i, j) - \bar{g}(i, j)]^2 \cdot \sum_{i=0}^{N-1} \sum_{j=0}^{M-1} [f(i, j) - \bar{f}(i, j)]^2}} \quad (3.8)$$

3.4.4 Correlation coefficient (CoC): The degree of adjustment or CoC is described by:

$$CoC = \left(\sum_m \sum_n (f_{mn} - \bar{f})(g_{mn} - \bar{g}) \right) / \sqrt{\left(\sum_m \sum_n (f_{mn} - \bar{f})^2 \right) \left(\sum_m \sum_n (g_{mn} - \bar{g})^2 \right)} \quad (3.9)$$

where \bar{f} and \bar{g} are the average values of the image, f_{mn} , g_{mn} images with the same size [44].

3.4.5 Structural content, SC is a measure based on correlation and is given by :

$$SC = \frac{\sum_{i=0}^{N-1} \sum_{j=0}^{M-1} (g(i, j))^2}{\sum_{i=0}^{N-1} \sum_{j=0}^{M-1} (f(i, j))^2} \quad (3.10)$$

3.4.6 Average Difference, AD indicates the average of the difference between the analyzed images:

$$AD = \frac{1}{N \cdot M} \sum_{i=0}^{N-1} \sum_{j=0}^{M-1} (g(i, j) - f(i, j)) \quad (3.11)$$

Capter IV

Anatomical-structural asymmetry and textural anisotropy of the brain

4.1 Quality and similarity metrics used in the analysis of anatomical-structural asymmetry

The values of the similarity metrics depend on the bi-lateral symmetry of the brain. In order to better highlight these brain hemisphere differences, some similarity metrics were computed: PSNR, MSE, NMAE, NCC, SC and AD.

4.2 Personal contributions

4.2.1 Structural brain asymmetry evaluated by histogram analysis and similarity metrics

The existence of structural asymmetry acts as a biomarker for the neuroanatomical disorders or abnormal brain functional organization. The development of a method based on histograms subtraction to highlight brain asymmetry using Diffusion-Weighted Magnetic Resonance Imaging (DW-MRI) may provide useful tools for differentiating between healthy and diseased subjects [16].

4.2.1.1 Histogram subtraction

The histogram difference of the left and right spitted hemispheres allows one to determine the distribution of the asymmetry. To obtain the left and right hemispheres, the localization of the mid-sagittal plane (MSP) is required. In order to find the sagittal axis, we maximized the location probability of the longitudinal fissure based on textural similarity analysis [17]. In this step, only intensity information is taken into account. It enhances the information about the changes in imaging conditions. After the histograms were created, a subtraction algorithm is used in order to obtain the difference of all pixel values at different bins. A normalized histogram of an image is defined as:

$$h_A(i) = \frac{n_i}{n}, i = \overline{0, 255} \quad (4.1)$$

where n_i is the number of pixels with gray level i and n is the total number of pixels in the image.

The subtraction result of two image histograms A and B is:

$$diff = \sum_i (h_A(i) - h_B(i)) \quad (4.2)$$

In order to quantify the differences, a subtraction algorithm between left and right brain histograms is used. Also, the following similarity indexes were computed: mean square error, peak signal to noise ratio, normalized cross correlation, average difference, structural content, and normalize absolute error.

The current study is carried out on 40 images from four subjects and for three b-values: 0, 500 and 1000 s/mm^2 , . Here, s/mm^2 is the attenuation factor and weights the diffusion.

Images denoted s1 belong to a healthy patient. Those denoted s2 belong to a patient with multiple intracerebral hemorrhages within the left temporal lobe; s3 with ischemic brain; and s4 is a subject with left frontoparietal brain abscess.

. Table 4.1 displays the quantitative results of the similarity metrics computed between left and right hemispheres of the brain. The quality values of these metrics are presented in table 4.2

Table 4.1 The similarity metrics computed between left and right hemispheres of the brain.

	b=0				b=500				b=1000			
	s1	s2	s3	s4	s1	s2	s3	s4	s1	s2	s3	s4
MSE	1.451	1.731	0.770	0.462	1.609	1.2452	1.544	0.476	1.506	1.591	1.827	0.877
PSNR	6.512	5.747	9.260	11.483	6.065	7.1784	6.238	11.358	6.354	5.1125	5.515	8.700
NCC	0.371	0.239	0.210	0.280	0.386	0.2590	0.198	0.297	0.374	0.2397	0.272	0.335
AD	-4.358	16.150	-2.639	-8.046	3.907	0.564	-4.049	-5.674	0.134	14.6341	9.942	-11.413
SC	0.944	1.269	0.929	0.682	1.050	1.0117	0.926	0.737	0.999	1.2436	1.071	0.668
NMAE	1.364	1.350	1.659	1.767	1.225	1.5108	1.712	1.627	1.293	1.3553	1.441	1.649

Table 4.2 The quality values of the similarity metrics.

Similarity metrics	Quality values
MSE	0
PSNR	higher
NCC	[-1, +1]
AD	0
SC	1
NAE	0


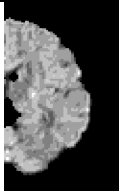
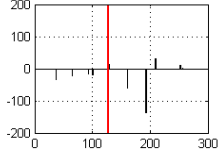
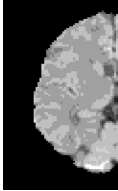
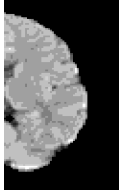
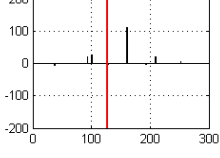
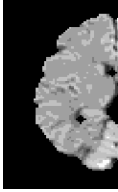

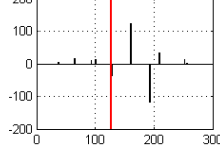
Table 4.1 shows significant differences between normal brain structures and various intracranial pathologies:

-PSN decreased with increasing b-value for all analyzed cases.

-Small NCC values indicate dissimilarity between brain hemispheres. The data reported in table 1 show differences between classes but also show an intra-class variation when the b-values increased (resulted images are brighter).

According to data in Table 4.3, for a normal brain a slight difference between the right and left hemispheres exists. This result indicates that the images from the healthy subject are, in a certain amount, degraded. One can interpret these differences in the light of the distortions during acquisition and processing. However, there is not much variation in the histogram-based intensity for subject s1, so we can expect that the histogram differences (as average intensity subtraction) could act as main tool in determining the ‘aberrations’ introduced by various diseases.

Table 4.3 Left and right hemispheres and histogram difference for s1

b[s/mm ²]	Right hemisphere	Left hemisphere	Histogram difference
b=0			
b=500			
b=1000			

Tables 4.4-4.6 show histogram differences for three diseases. The existing asymmetry increases the absolute difference due to the distortion of the gray level intensity. The differences between histograms are declared if the absolute differences of the gray level intensity between left and right hemispheres is greater than the threshold $T = 126$. This threshold value was obtained using Otsu’s thresholding algorithm.

Table 4.4 Left and right hemispheres and histogram difference for s_2



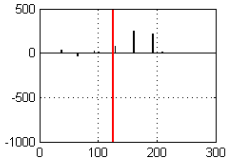


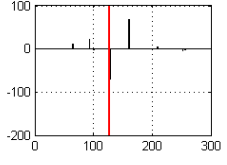


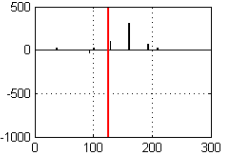
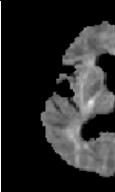
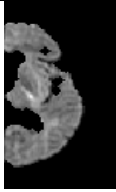
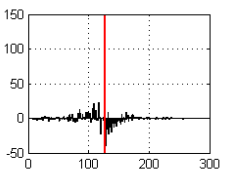


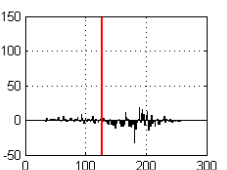
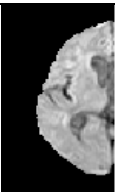
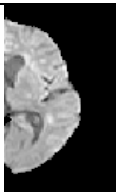
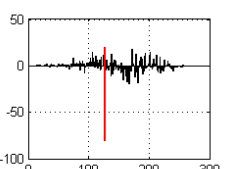
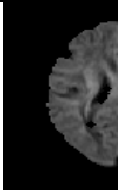
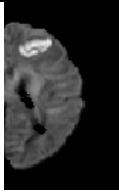
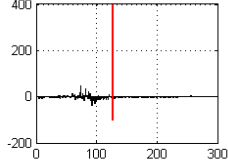
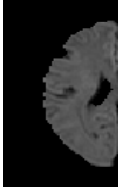
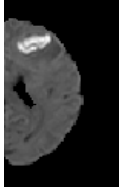
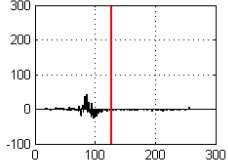
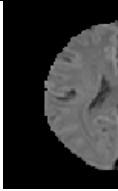
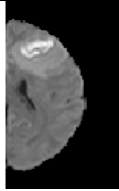
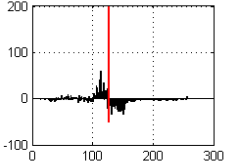
$b[s/mm^2]$	Right hemisphere	Left hemisphere	Histogram difference
$b=0$			
$b=500$			
$b=1000$			

Table 4.5 Left and right hemispheres and histogram difference for s_3 .

$b[s/mm^2]$	Right hemisphere	Left hemisphere	Histogram difference
$b=0$			
$b=500$			
$b=1000$			

4.2.2 Entropic characterization of random cerebral structures in MR images using structural similarity studies

Table 4.6 Left and right hemispheres and histogram difference for $s4$

$b[s/mm^2]$	Right hemisphere	Left hemisphere	Histogram difference
$b=0$			
$b=500$			
$b=1000$			

The data reported in this section were published in [45] L. Moraru, L. T. Dimitrievici, V. A. Moraru, Structural brain asymmetry evaluated by histogram analysis and similarity metrics, Annals Of “Dunarea De Jos” University Of Galati Mathematics, Physics, Theoretical Mechanics Fascicle II, Year VIII (XXXIX), No. 1, pp 13-19, 2016.

4.2.2 Entropic characterization of random cerebral structures in MR images using structural similarity studies

The analysis of pixel distribution offers a perspective on the changes existing in the level of the microstructure of the brain tissue. The purpose of the research was to correlate the perturbation / disorder of the pixels at the micro and macroscopic level with the type of image and the type of disease. The quantification of the degree of disorder in brain microstructures can be estimated by texture analysis [18].

FSIM and SSIM indices can detect relatively similar / non-similar patterns in brain MRI images, using spatial inhomogeneity and spatial statistical complexity of gray tones, from images.

4.2.2.1 SSIM and FSIM

Two images I and J are characterized by the mean μ_I, μ_J , variance σ_I^2, σ_J^2 and covariance σ_{IJ} . The luminance $l(I, J)$, contrast $c(I, J)$, and structural $s(I, J)$ similarity components are defined as :

$$l(I, J) = \frac{2\mu_I\mu_J + C_1}{\mu_I^2 + \mu_J^2 + C_1}, \quad c(I, J) = \frac{2\sigma_I\sigma_J + C_2}{\sigma_I^2 + \sigma_J^2 + C_2}, \quad s(I, J) = \frac{\sigma_{IJ} + C_3}{\sigma_I\sigma_J + C_3} \quad (4.3)$$

where C_1, C_2 and C_3 are small constants used to avoid an indeterminate form (if denominators approached 0). The positive parameter α, β and γ are used to adjust the relative importance of the components and the SSIM index is defined as [18]:

$$SSIM(I, J) = [l(I, J)]^\alpha [c(I, J)]^\beta [s(I, J)]^\gamma \quad (4.4)$$

For FSIM calculation are determined PC (The phase congruency feature which is contrast invariant) and G (gradient magnitude which encodes contrast information) for both images I and J for a location x . The similarity measures for phase congruency and gradient magnitude are defined as [19]:

$$S_{PC}(x) = \frac{2PC_I(x) \cdot PC_J(x) + \varepsilon_1}{PC_I^2(x) + PC_J^2(x) + \varepsilon_1}, \quad S_G(x) = \frac{2G_I(x) \cdot G_J(x) + \varepsilon_2}{G_I^2(x) + G_J^2(x) + \varepsilon_2} \quad (4.5)$$

FSIM index is given by [76]:

$$FSIM = \frac{\sum_{x \in \Omega} S_L(x) \cdot PC_m(x)}{\sum_{x \in \Omega} PC_m(x)} \quad (4.6)$$

4.2.2.2 The entropy

Entropy is a statistical measure of randomness that can be used to characterize the texture of the image. Entropy, as a local morphological descriptor systematically characterizes the random microstructures. For a 2D grey image having N pixels (discretized into scale from 0 to 255 intensity levels), and $h_i(i)$ being the normalized histogram image, the image entropy is given by [19-20]:

$$H(I) = -\sum_i h_i(i) \log N/h_i(i) \quad (4.7)$$

The dataset consists of stacks of PDw brain MR images which were freely downloaded from the website of Harvard Medical School. The abnormal brain MR images consist of the following diseases: Alzheimer's disease, Pick's disease, and cerebral calcinosis. The samples of each image type and disease are illustrated in Figure 4.1:

4.2.2 Entropic characterization of random cerebral structures in MR images using structural similarity studies

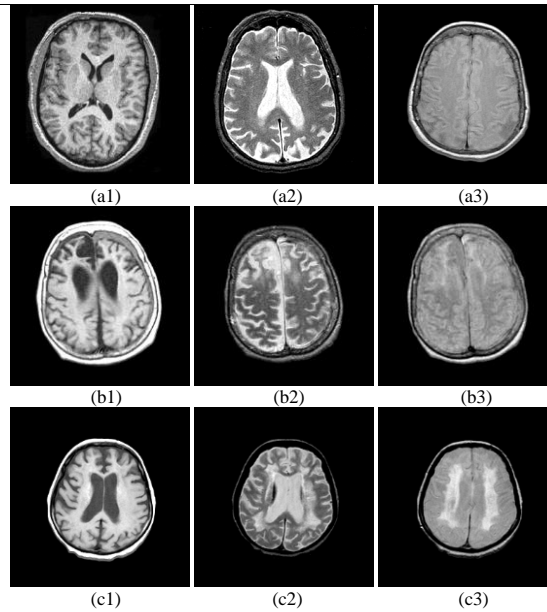


Figure 4.1 The images represent: (a) Alzheimer's disease; (b) Pick's disease; (c) Cerebral calcinosis disease. Columns: (1) - T1w images; (2) T2w images; (3) PDw images of a figure caption.

The colour imaging system red, green and blue (RGB) is used to check and highlight the existing differences at microstructural level between two successive images.

However, it is possible to ignore one of the channels of information because the data size is drastically reduced and the processing time is improved. The R and G channels are suitable for our goal. The B channel has been ignored in our analysis. The results are provided in a three steps sequence:

(1) The differences between two consecutive images of chosen neurodegenerative diseases, in a colour approach have been made in figure 4.2. Figures denoted with (c) illustrate the existing differences at microscopic level in cerebral structures by using the R and G channels from RGB colour model. The similar areas appear yellow. The number of pixels varies from one image to the next one.

Figures 4.3 and 4.4 show the variation of the number of pixels that do not overlap depending on the R and G channels. The number of pixels that do not overlap decreases as the index of image pairs increases. Images denoted c1, c2 and c3 are RGB composite images that show differences between pixels (for red and green channels) in images 4.3 and 4.4.

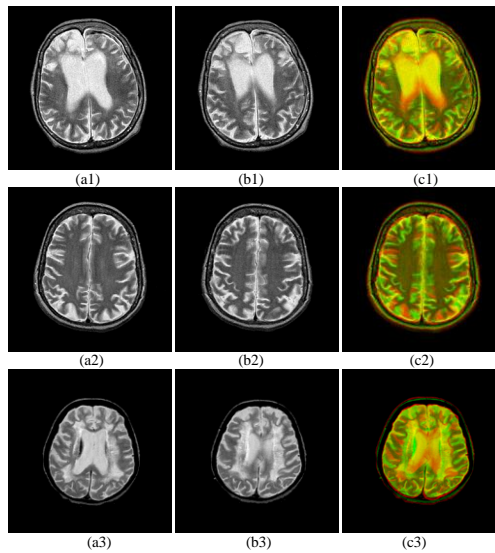


Figure 4.2 Colour comparison between two T2w consecutive images (the first and second columns); (a) PDis; (b) ADIs; (c) CCDIs. The similar areas appear yellow.

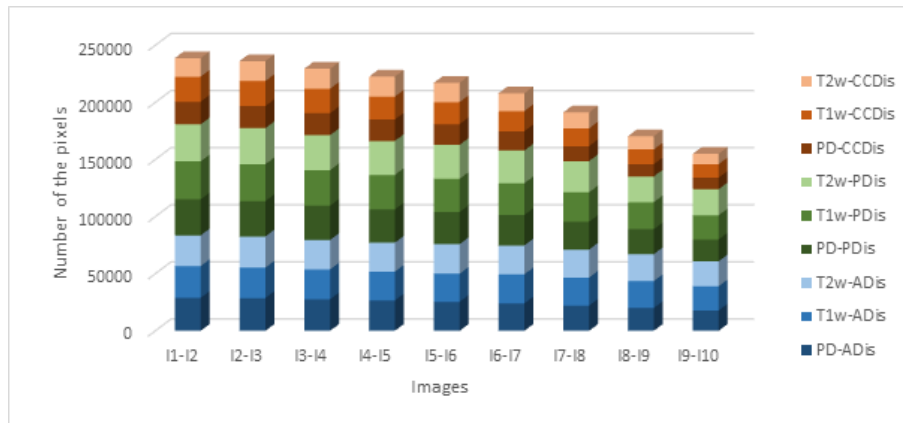


Figure 4.3 The evolution of the number of non-overlapping pixels belonging to the R channel

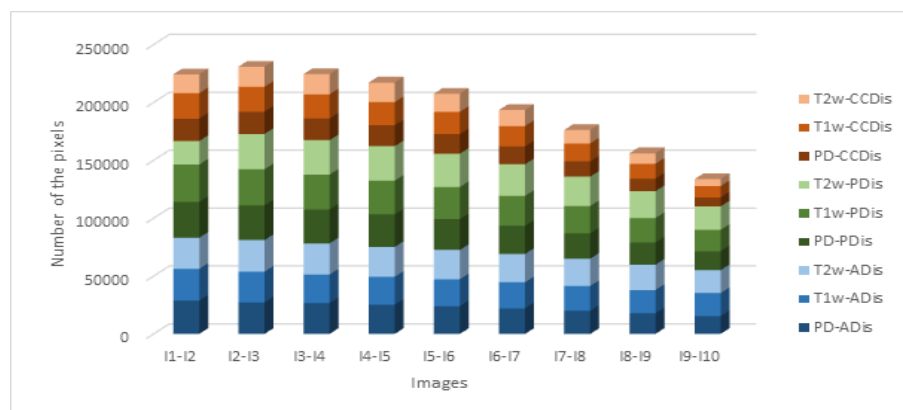


Figure 4.4 The evolution of the number of non-overlapping pixels belonging to the G channel

4.2.2 Entropic characterization of random cerebral structures in MR images using structural similarity studies

Table 4.7 average values of the entropy for neurogenerative diseases

	Alzheimer's disease	Cerebral calciosis disease	Pick's disease
PDw	3.928 (± 0.490)	3.840 (± 0.495)	3.534 (± 0.481)
T1w	3.181 (± 0.507)	3.411 (± 0.492)	3.031 (± 0.504)
T2w	2.399 (± 0.249)	3.676 (± 0.491)	2.294 (± 0.400)

(2) The entropy values corresponding to the image stack associated with each disease are calculated. The average values of the entropy results are presented in table 4.7.

(3) A similarity study is performed from successive pair images using SSIM and FSIM. The results are shown in Figure 4.5.

In the composite image presented in figures 4.2c, the yellow areas indicate the same intensities in the input images. The dissimilar pixels are labeled with red and green and show those areas where the pixel intensities are different. This comparison reveals that the microstructural differences between arrangements of white and grey pixels yield a higher compositional inhomogeneity. For each image type and neurodegenerative disease, the number of non-overlapping pixels was established, for both the R and G channels (see Figures 4.3 and 4.4). The number of non-overlapping pixels (quantified by the area of a microscopic region where structural differences exist) shows a clear trend; it decreases towards increasing the index of the image pairs.

The smallest area is occupied by pixels belonging to the R channel in the case of T2w-PDis, and the biggest area is occupied by pixels belonging to the G channel for T2w-CCDis. Hence, we can preliminary conclude that the microstructural morphology is heterogeneous and clearly varies from case to case. In the case of T1w images, the dissimilarity degree is the smallest because the differences of local contrast between grey and white matter are not important. For T2w images, the local contrast increases for cerebrospinal fluid area and, accordingly, the SSIM values increase. SSIM takes values in the range [0.85; 0.93] for CCDIs, [0.66; 0.89] for ADIs and [0.69; 0.87] for PDis, respectively.

FSIM also confirms the existing dissimilarity in the sequence from the stack of images (Fig. 4.5, right column). Generally, the FSIM shows the same evolution as SSIM. Few exceptions exist for T1w and T2w images when FSIM values overlap the SSIM values. FSIM takes values in the range [0.68; 0.82] for CCDIs, [0.57; 0.74] for ADIs and [0.54; 0.75] for PDis, respectively.

The values of the SSIM (left column) for PDw images are higher than those of T1w and T2w images for all diseases. Also, the degree of the dissimilarity increases for the last pairs of images in the stack.

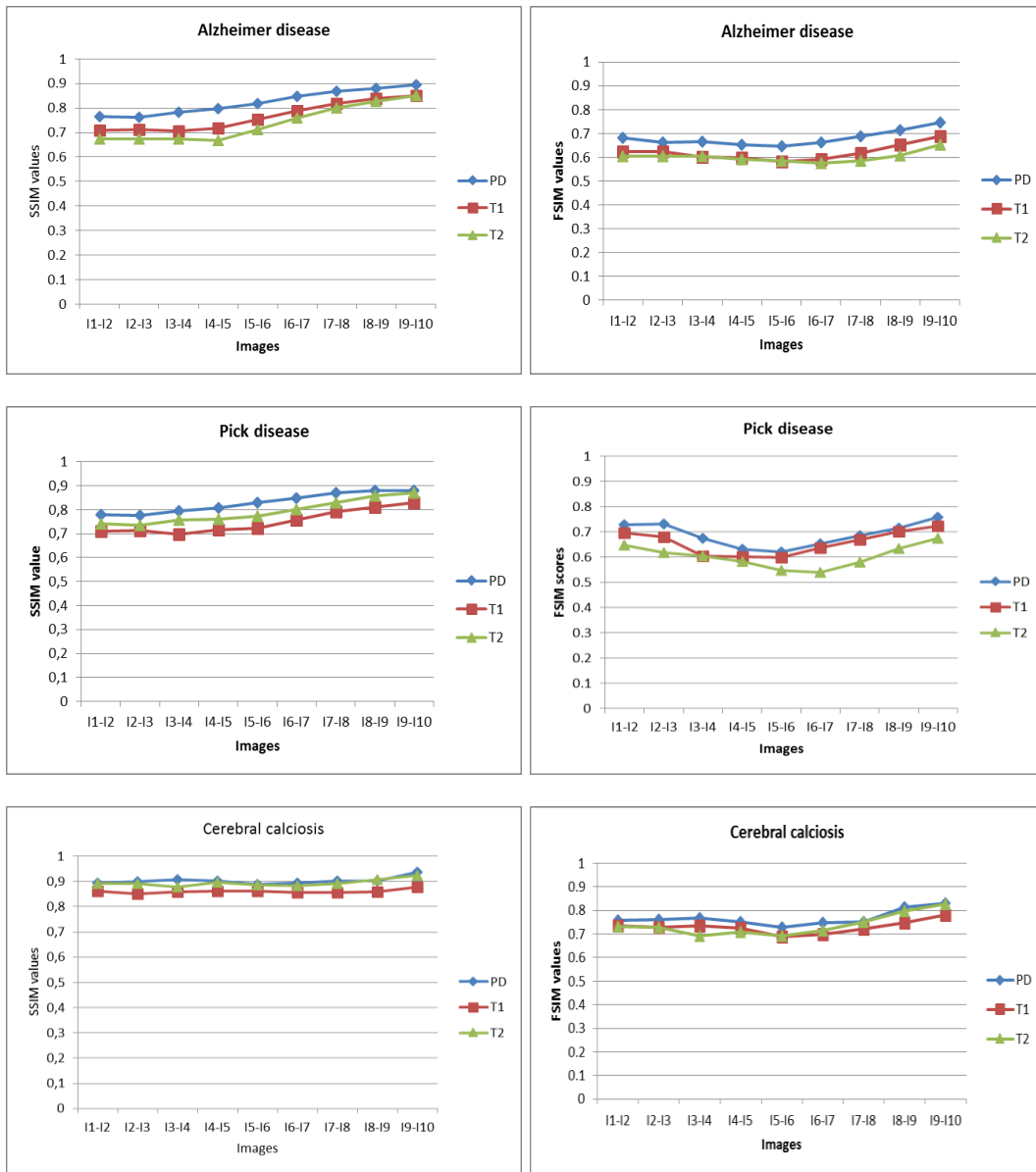


Figure 4.5 The dissimilarity index values of paired images for various degenerative diseases. Left column: SSIM. Right column: FSIM.

The entropy as a measure of information is closely related to the grey level distribution and its estimation is based on probability distributions of the intensities of pixels and on the locally spatial similarity of pixel intensities within neighborhoods. The higher entropy values for PDw images (Table 1) express that this disease introduces the higher disorder at microscopic level reflecting the pixels' disorder. Also, entropy provides information on how homogeneous a class is, because it tends to zero when all pixels belong to the same class, i.e. have the same grey level. In this case, Pick's disease has the most homogeneous structure, and the cerebral calcification disease has a heterogeneous microstructure.

4.2.3 Texture anisotropy methods in brain degenerative diseases investigation

In this study the investigated area is reduced from the whole brain surface to three major lobes (i.e. frontal, temporal and parietal). [27]. A database containing 105 brain two-dimensional MR images was included in the proposed work. The acquired images were T2w and PD (proton density) sequences that belong to the Harvard Medical School database, which are available at [25]. The existing study included 28 images of healthy patients (as control group), and 77 MR images (29 AD patients, 24 PD patients, and 24 CC patients).

The cerebral calcinosis (CC) is characterized by abnormal deposits of calcium in certain areas of the brain (mostly in the FL, TL and PL) and may include similar clinical symptoms with the AD and PD. Unlike AD and PD, the CC does not manifest atrophy, but induces signal intensity alteration.

The proposed statistical model avoids 'the human ground truth' based on human understanding of topographical and morphological imaging changes or experience of clinical symptoms. Thus, in the proposed model, for model evaluation free of human biases, the CC represented an artificial ground truth, and its relevance is used. For statistical analysis, the database was organized into the following classes: healthy patients (H), Alzheimer (A), Pick (P) and cerebral calcinosis (CC).

4.2.3.1 Non-local means filter (NLM)

The non-local means (NLM) filter reduces the noise without damaging textures and fine structures. Furthermore, it calculates the mean of all pixels in the image. In addition, it weights those pixels that exceed the calculated mean value and removes the Rician noise

4.2.3.2 Co-occurrence matrix CM describe the spatial complexity of the images and the variation in directions for pixel pairs[23]

4.2.3.3 Morlet Wavelet transform (WM) belongs to the class of directional wavelet and is used to test the existence of anisotropy, because it can detect the uneven changes in the texture of the images. [24].

4.2.3.4 Hessian operators

A structure tensor in a two-dimensional (2D) image representation is defined using a 2×2 Hessian matrix [27]:

$$H(I(x, y)) = \begin{bmatrix} I_{xx} = \frac{\partial^2 I(x, y)}{\partial x^2} & I_{xy} = \frac{\partial^2 I(x, y)}{\partial x \partial y} \\ I_{yx} = \frac{\partial^2 I(x, y)}{\partial y \partial x} & I_{yy} = \frac{\partial^2 I(x, y)}{\partial y^2} \end{bmatrix} \quad (4.11)$$

4.2.3.5 Statistical analysis

The proposed statistical model involves the following steps:

Start

Remove the Rician noise by using the NLM filter

Segment the skull stripping

Use the irrational mask method for segmentation

Assess the skull-stripping method performance by means of the Dice coefficient

Analyze the texture anisotropy based on the CM and the WM

Compute the TA of the whole brain and major lobes, respectively.

Assess the statistical significance of anisotropy values for the analyzed classes at a specified localization.

Use the paired t-test to determine whether the mean of the texture anisotropy differences is statistically significant.

Calculate the Pearson's correlations coefficient for the effect of TA and clinical status by applying the association analysis.

Obtain the model output that contains only those significant classes that have the ability to reduce the area of analysis from the whole brain surface to the major lobes.

Address the consistency index to summarize the relevance of the texture anisotropy analysis over its range of values for all analyzed classes, all image types and all analyzed areas.

Evaluate the proposed method via unbiased assessment of the model

End

The information on texture anisotropy provided by the CM is supplemented by those provided by the MW based on the variation in directions for pixel pairs (CM), and for a chosen orientation (MW).

The data for homogeneity, correlation and energy features is summarized in Figure 4.6 showing not classes with the zero TA variation. The texture of the brain MR images has an anisotropic character. By comparing the range of TA variation for each feature, image type, and pathology higher variation for the T2w images than for PD images is obtained. In addition, a major difference in TA associated with investigated area exists

For class Ad, the energy and correlation overall results indicate that the texture is strongly inhomogeneous and contains various discontinuities such as edges. These directional attributes of the CM suggest that anisotropy could be a marker of increased cerebral atrophy and of disease progression.

4.2.3 Texture anisotropy methods in brain degenerative diseases investigation

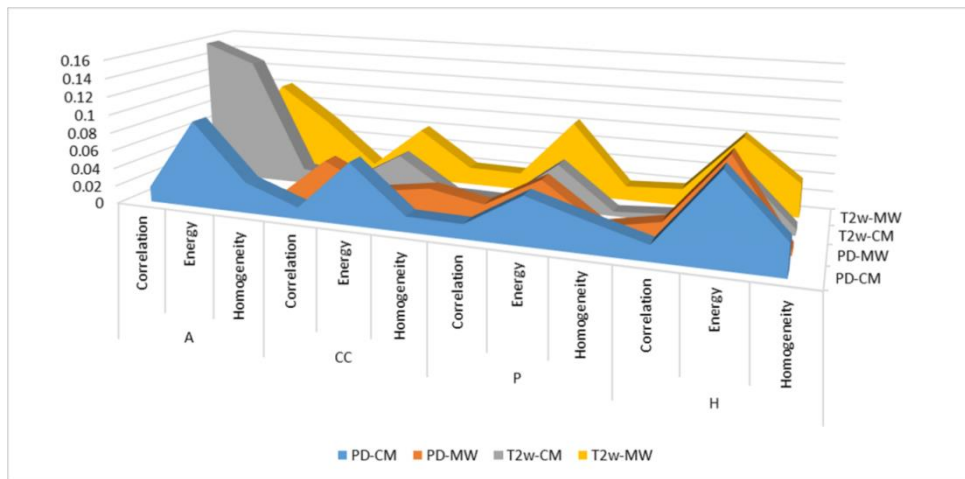


Figure 4.6 Range of variation for correlation, energy and homogeneity computed using CM and MW for PD and T2w images

According to data in Table 4.8, it is established that in WB and TL the anisotropy is higher (corresponding to less ordered texture) than in FL and PL.

Table 4.8. Multivariate analysis between disease classes and ROI based on the anisotropy showing the correlation intensity

WB		FL		TL		PL	
PDw	T2w	PDw	T2w	PDw	T2w	PDw	T2w
H-A	H-A	H-A	H-A**	H-A	H-A	H-A	H-A
H-P	H-P	H-P**	H-P	H-P*	H-P	H-P	H-P*
H-CC**	H-CC*	H-CC	H-CC*	H-CC	H-CC	H-CC	H-CC
A-P	A-P	A-P	A-P	A-P	A-P	A-P**	A-P
A-CC**	A-CC	A-CC	A-CC**	A-CC*	A-CC	A-CC	A-CC**
P-CC**	P-CC**	P-CC	P-CC	P-CC	P-CC**	P-CC	P-CC

(*) moderately strong correlation and VIF < 5

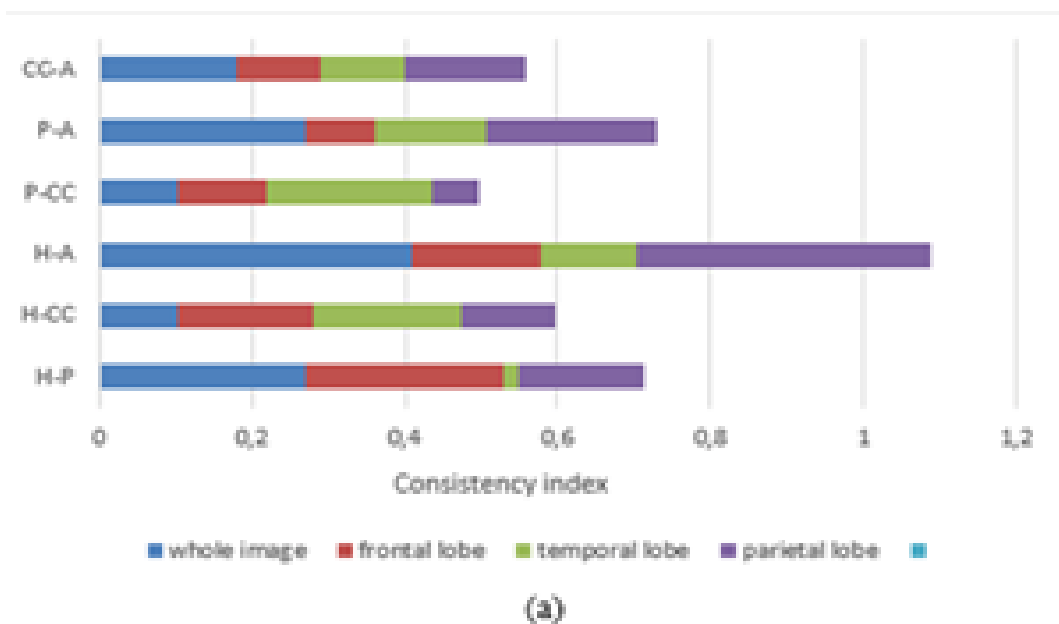
(**) very strong correlation and VIF > 5 (are not used in the proposed model)

The average values of anisotropy and their standard deviations are illustrated in the Table 4.9.

Table 4.9 Average anisotropy (\pm standard deviation) values for each image type and investigated areas

Classes	Investigated area				
	Image type	WB	FL	TL	PL
Ad	PDw	0,453(\pm 0,190)	0,159(\pm 0,089)	0,505(\pm 0,168)	0,316(\pm 0,157)
	T2w	0,178(\pm 0,195)	0,174(\pm 0,084)	0,380(\pm 0,155)	0,280(\pm 0,149)
CCd	PDw	0,407(\pm 0,177)	0,261(\pm 0,170)	0,550(\pm 0,209)	0,226(\pm 0,127)
	T2w	0,216 (\pm 0,097)	0,258 (\pm 0,170)	0,445(\pm 0,098)	0,188(\pm 0,099)
Pd	PDw	0,372(\pm 0,116)	0,230(\pm 0,109)	0,503(\pm 0,127)	0,191(\pm 0,089)
	T2w	0,167 \pm (0,089)	0,118(\pm 0,043)	0,408(\pm 0,106)	0,160(\pm 0,053)
H	PDw	0,054(\pm 0,026)	0,175 (\pm 0,031)	0,525(\pm 0,134)	0,118(\pm 0,051)
	T2w	0,055(\pm 0,026)	0,139(\pm 0,065)	0,415(\pm 0,106)	0,180(\pm 0,072)

During the second step of the decision process, the accuracy of the selection has been estimated using the consistency index (Figure 4.7). It demonstrates the relevance of the selected variables by the proposed model.



4.2.3 Texture anisotropy methods in brain degenerative diseases investigation

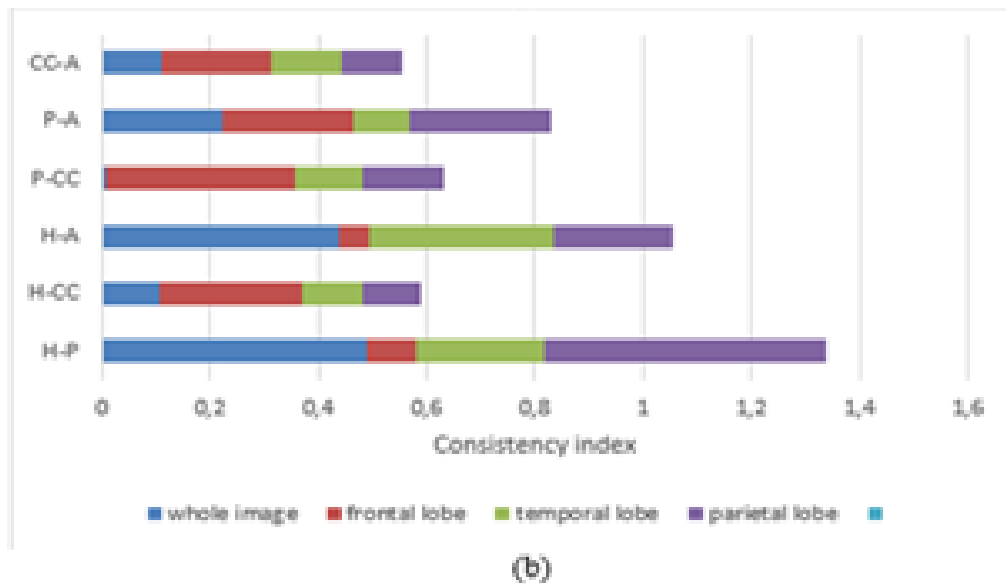


Figure 4.7 Consistency index: (a) PD images; (b) T2w images.

Table 4.10 demonstrates that the training dataset provides higher AUC values, while the AUC for validation data set were lower. The Ad and Pd diseases have the highest AUC among the classes tested. The training step is the prerequisite to any decision to undertake a between-diseases classification test or to discriminate the true state of patients.

Table 4.10 Area under the ROC curve (The highlighted values indicate the cases where anisotropy is unable to distinguish between classes)

Diseases	WB		FL		TL		PL	
	PDw	T2w	PDw	T2w	PDw	T2w	PDw	T2w
Ad training	0.852 ^{b)}	0.859 ^{b)}	0.874 ^{b)}	0.911 ^{a)}	0.890 ^{b)}	0.812 ^{b)}	0.606 ^{d)}	0.909 ^{a)}
Ad validation	0.802 ^{b)}	0.810 ^{b)}	0.813 ^{b)}	0.877 ^{b)}	0.853 ^{b)}	0.780 ^{c)}	0.585 ^{f)}	0.883 ^{b)}
Pd training	0.598 ^{f)}	0.482 ^{f)}	0.880 ^{b)}	0.608 ^{d)}	0.753 ^{c)}	0.866 ^{b)}	0.727 ^{c)}	0.784 ^{c)}
Pd validation	0.537 ^{f)}	0.457 ^{f)}	0.833 ^{b)}	0.563 ^{f)}	0.707 ^{c)}	0.822 ^{b)}	0.690 ^{d)}	0.733 ^{c)}
CCd training	0.245 ^{f)}	0.222 ^{f)}	0.176 ^{f)}	0.329 ^{f)}	0.204 ^{f)}	0.198 ^{f)}	0.346 ^{f)}	0.377 ^{f)}
CCd validation	0.223 ^{f)}	0.205 ^{f)}	0.153 ^{f)}	0.313 ^{f)}	0.190 ^{f)}	0.183 ^{f)}	0.328 ^{f)}	0.357 ^{f)}
H training	0.786 ^{c)}	0.79 ^{c)}	0.873 ^{b)}	0.804 ^{b)}	0.744 ^{c)}	0.688 ^{d)}	0.940 ^{a)}	0.785 ^{c)}
H validation	0.737 ^{c)}	0.745 ^{c)}	0.817 ^{b)}	0.747 ^{c)}	0.697 ^{d)}	0.650 ^{d)}	0.890 ^{b)}	0.730 ^{c)}

a) 0.90-1 = excellent, b) 0.80-0.90 = very good c) 0.70-0.80 = good, d) 0.60-0.70 = fair, f) 0-0.60 = fail.

Table 4.11 summarizes the sensitivity and specificity values computed from the cut-off values of the ROC. The sensitivity is the proportion of patients with a diagnosed brain disease who are correctly identified by anisotropy. The specificity refers to the ability of the texture anisotropy to correctly identify negative among those patients without the disease

According to the recommendations in [38], sensitivity higher than 80 is required % for detecting the targeted disease, in addition higher specificity of 80% is necessary for distinguishing other dementias. The cut-off values were selected for the range of sensitivity of clinical importance (i.e. between 90% and 100%).

Table 4.11 Sensitivity and Specificity values of the proposed model (95% confidence interval)

Diseases	FL		TL		PL	
	PDw	T2w	PDw	T2w	PDw	T2w
Ad	(0,91; 0,80)	(0.90; 0.82)	(0.90; 0.82)	(0.91; 0.67)	(0.84; 0.67)	(0.89; 0.87)
Pd	(0.93; 0.81)	(0.81; 0.37)	(0.86; 0.69)	(0.88; 0.71)	(0,84; 0.67)	(0.80; 0.79)
H	(0.92; 0.82)	(0.91; 0.79)	(0.94; 0.86)	(0.90; 0.73)	(0.88; 0.79)	(0.91; 0.81)

Alzheimer’s disease shows the highest sensitivity (> 90%) for both FL and TL for both image types. Also, PL and T2w image has almost the same sensitivity. Pick’s disease has sensitivity from 80% to 90%. The specificity is higher for Alzheimer’s disease. This indicates that the proposed model is correctly report >80% patients without Alzheimer’s disease when FL and TL are addressed. In the case of the Pick’s disease, for FL/T2w, the lower values of specificity indicate 37% patients without P disease are incorrectly detected positive and the model ability to identify this disease is compromised. This instance was already removed from the proposed model. Overall, specificity varied between 0.69 and 0.81 over the same sensitivity range. It is fair enough to estimate how likely patients without disease can be correctly ruled out.

The main challenge in the proposed model is the minimization of the analyzed brain area, while still achieving a high classification rate. It is a merit of the proposed model to statistically distinguish between Alzheimer’s and Pick’s diseases when basically the same types of imaging data are required to develop this model.

The data reported in this study were published in [30] L. Moraru, S. Moldovanu, L. T. Dimitrievici, N. Dey, A. S. Ashour, Texture Anisotropy technique in Brain Degenerative Diseases, *Neural Computing and Applications*, Volume 30, Issue 5, pp1667-1677, DOI: 10.1007/s00521-016-2777-7, september 2018.

4.2.4 Gaussian mixture models (GMM) for brain DTI texture characterization

4.2.4 Gaussian mixture models (GMM) for brain DTI texture characterization

A GMM is a probabilistic model based on Gaussian distribution for expressing the presence of sub-populations/sub-classes within an overall population/class without requiring the identification of the subclass of interest (observational data).

4.2.4.1 Methodological approach

4.2.4.2 The GMM algorithm with m components

The finite mixture model is based on the assumption that each finite mixture has similar probability distributions for each group; however, inside the group, different multivariate probability density distributions and different parameters are present [31,32].

4.2.4.3 The k-means algorithm for clustering

The k-means algorithm is used to assess the data clustering for the selected number of components ($m = 3$) [26, 27]. Each mixture component is associated with a group or cluster based on identical estimated statistical parameters.

4.2.4.4 Euclidian weighted distance and multiple correlation

To validate the capability of the classified GMM mixtures to differentiate between different subjects in a hemisphere approach, the weighted Euclidean distance (wd) between two j -dimensional vectors was used [34]:

$$wd_{H-IS}^j = \sqrt{\sum_j \left(\frac{w_{ij}^H}{s_j^H} - \frac{w_{ij}^{IS}}{s_j^{IS}} \right)^2} \quad \text{și} \quad wd_{H-HA}^j = \sqrt{\sum_j \left(\frac{w_{ij}^H}{s_j^H} - \frac{w_{ij}^{HA}}{s_j^{HA}} \right)^2} \quad (4.15)$$

where w_{ij} ($i = 1, 2, 3$ și $j = \overline{1, n}$) denotes the optimal mixture probability provided by k-means for the studied subclasses and s_j is the corresponding standard deviation.

Moreover, an inter-hemisphere multiple correlation analysis between the mixing probabilities has been performed to characterize the association of the grey level intensities and contrast for the selected injured subjects and healthy subject. The multiple correlation coefficients between the independent variables HA and IS and the dependent variable H is defined as

$$R_{H-(IS,HA)}^i = \sqrt{\frac{(r_{IS,H}^i)^2 + (r_{HA,H}^i)^2 - 2r_{IS,H}^i r_{HA,H}^i r_{IS,HA}^i}{1 - (r_{IS,HA}^i)^2}} \quad (4.16)$$

Where $r_{IS,H}^i, r_{HA,H}^i, r_{IS,HA}^i$ $i = 1,2,3$ are the covariance between the two random variables in each of the pairs IS and H , HA and H and IS and HA , respectively [35].

4.2.4.5 Clustering validation

The analysis is focused on three main brain tissues (i.e., GM, WM, and CSF), and an a priori assumption of three-class clustering is considered. The goal is to examine whether these classes reflect the actual clustering structure of the data or whether this data was partitioned into a few artificial groups, in the context of the GMM [36]. The quality of the clustering analysis is addressed, and the Silhouette index and Silhouette plots are used as the validation criteria [38]. If compact and clearly separated clusters are obtained, the targeted tissues were considered well-classified. The Algorithm diagram is shown in Figure 4.8:

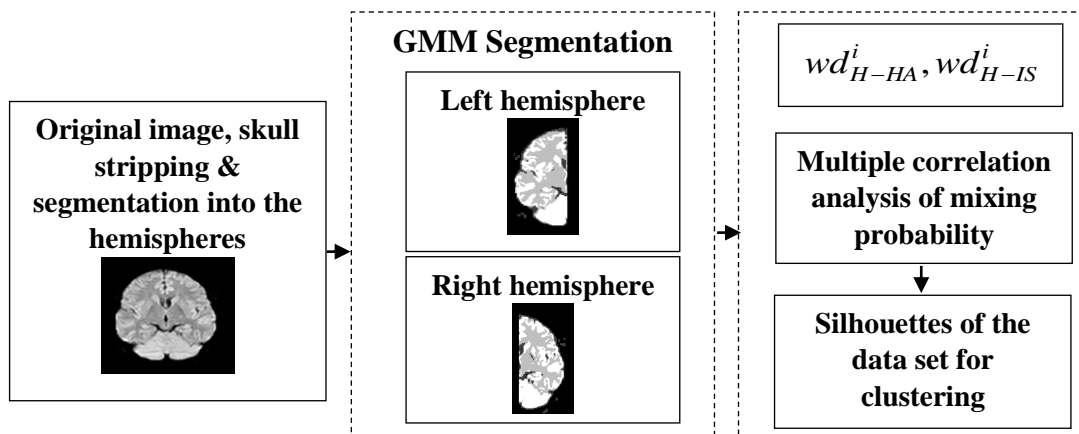


Figure 4.8 Algorithm scheme

4.2.4.6 Image acquisition and processing

Three subjects (age range 36–60 y; one female and two males) underwent MRI scans. A subject presented multiple haemorrhage areas in the left temporal lobe (male, 48 y), and another was with ischemic stroke in the left frontal lobe (female, 60 y, median 8-mo post-stroke); yet another subject was a healthy patient (male, 36 y).

As an example, a DTI image ($b = 500 \text{ s/mm}^2$) of a healthy subject and the results of the GMM-classification and hemisphere segmentation are shown in Fig. 4.9.

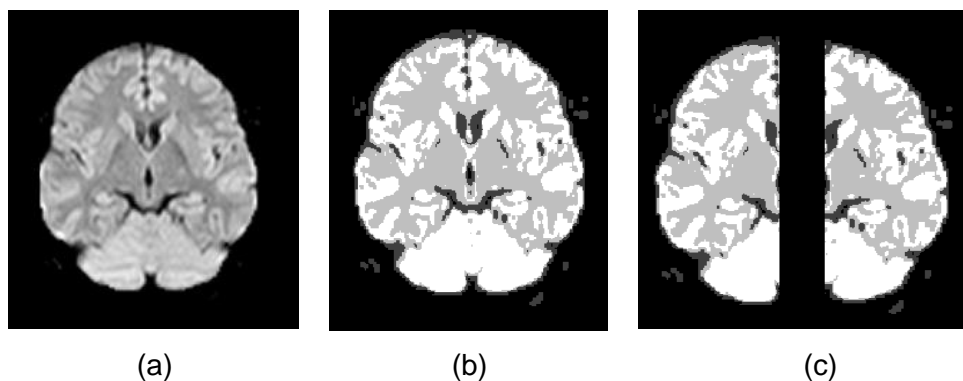


Figure 4.9 DTI brain image of a healthy patient for $b = 500 \text{ s/mm}^2$. (a) skull stripping of the whole brain; (b) result of GMM-classification; (c) hemispheres segmentation

4.2.4 Gaussian mixture models (GMM) for brain DTI texture characterization

The estimated weights across the entire control group (H) and for each injured group (IS and HA) are presented in Table 4.12 (for the left hemisphere) and Table 4.13 (for the right hemisphere). The data in Tables 4.12 and 4.13 present details on the difference in the averaged weights or mixing probabilities between the left and right hemispheres for each subject and over the entire range of diffusion gradient values.

Table 4.12 GMM average mixing probability for left hemisphere, with and without diffusion gradients. The data are summarized for three mixing probabilities

(w1 for GM, w2 for WM and w3 for CSF) for H, HA and IS.

	$\langle w_1 \rangle \pm s_j^H$	$\langle w_1 \rangle \pm s_j^{HA}$	$\langle w_1 \rangle \pm s_j^{IS}$	$\langle w_2 \rangle \pm s_j^H$	$\langle w_2 \rangle \pm s_j^{HA}$	$\langle w_2 \rangle \pm s_j^{IS}$	$\langle w_3 \rangle \pm s_j^H$	$\langle w_3 \rangle \pm s_j^{HA}$	$\langle w_3 \rangle \pm s_j^{IS}$
b0	0.30±0.012	0.26 ±0.008	0.22±0.014	0.55±0.049	0.58±0.048	0.55±0.064	0.14±0.045	0.15±0.045	0.17±0.061
b250	0.32±0.021	0.30±0.017	0.29±0.020	0.52±0.046	0.52±0.051	0.54±0.059	0.14±0.051	0.15±0.051	0.15±0.047
b500	0.32±0.027	0.30±0.020	0.29±0.021	0.52±0.056	0.54±0.057	0.55±0.048	0.14±0.045	0.15±0.047	0.15±0.051
b750	0.33±0.023	0.29±0.023	0.29±0.021	0.54±0.015	0.55±0.052	0.56±0.053	0.13±0.007	0.15±0.042	0.15±0.041
b1000	0.32±0.021	0.29±0.020	0.29±0.019	0.52±0.048	0.55±0.053	0.55±0.058	0.14±0.050	0.15±0.052	0.15±0.048
b1250	0.33±0.025	0.28±0.018	0.28±0.016	0.55±0.059	0.55±0.055	0.55±0.056	0.14±0.044	0.15±0.050	0.15±0.049

Table 4.13 GMM average mixing probability for right hemisphere, with and without diffusion gradients. The data are summarized for three mixing probabilities

(w1 for GM, w2 for WM and w3 for CSF) for H, HA and IS.

	$\langle w_1 \rangle \pm s_j^H$	$\langle w_1 \rangle \pm s_j^{HA}$	$\langle w_1 \rangle \pm s_j^{IS}$	$\langle w_2 \rangle \pm s_j^H$	$\langle w_2 \rangle \pm s_j^{HA}$	$\langle w_2 \rangle \pm s_j^{IS}$	$\langle w_3 \rangle \pm s_j^H$	$\langle w_3 \rangle \pm s_j^{HA}$	$\langle w_3 \rangle \pm s_j^{IS}$
b0	0.32±0.016	0.33±0.018	0.28±0.013	0.54±0.041	0.53±0.050	0.57±0.039	0.12±0.032	0.13±0.041	0.14±0.048
b250	0.34±0.022	0.33±0.041	0.30±0.021	0.51±0.053	0.53±0.051	0.53±0.059	0.14±0.045	0.13±0.044	0.15±0.047
b500	0.34±0.022	0.34±0.029	0.30±0.028	0.50±0.050	0.51±0.059	0.52±0.055	0.14±0.045	0.14±0.044	0.15±0.050
b750	0.35±0.016	0.34±0.029	0.28±0.023	0.52±0.007	0.48±0.042	0.52±0.041	0.13±0.039	0.13±0.039	0.16±0.043
b1000	0.33±0.018	0.33±0.029	0.30±0.029	0.51±0.054	0.51±0.060	0.53±0.055	0.14±0.044	0.14±0.045	0.15±0.047
b1250	0.34±0.019	0.33±0.026	0.30±0.023	0.54±0.053	0.51±0.057	0.51±0.061	0.14±0.044	0.14±0.045	0.15±0.046

For two cases (multiple haemorrhage areas in the left temporal lobe (HA) and ischemic stroke in the left frontal lobe (IS)), visible differences in the mixing probabilities are presented.

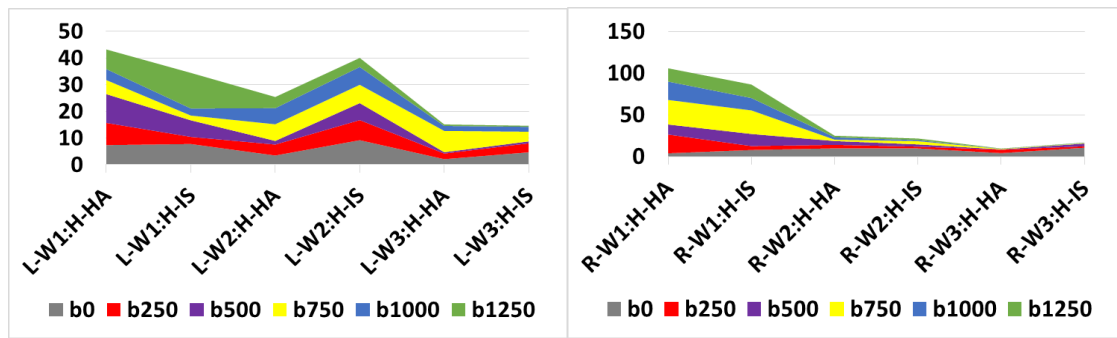


Figure 4.10 Average weighted Euclidean distances for pairs of probability density function distributions of mixtures probability of GMM. Estimation is performed for all the diffusion gradients and for each brain hemisphere. L denotes the LH, R denotes the RH.

Figure 4.10 indicates that the proposed approach exhibits the capability to highlight the differences between the brain tissues in the right and left hemispheres, for each level of diffusion weighting and subject category.

For the CSF class (index 3), HA and IS do not correlate significantly with H for either the left or right hemispheres. The results for the WM class (index 2) illustrate that for the left hemispheres, HA and IS are marginally correlated with H. The correlation significance increases by approximately 50% for the right hemispheres. For the GM class (index 1), HA and IS correlate well with H for the right hemisphere and do not correlate significantly with H for the left hemisphere.

The average silhouette width is approximately 0.9, i.e., 90 % of the selected clusters are considered as the optimal number of clusters (table 4). The a priori selection of the three main brain tissues, or ‘natural determination’, is validated and performs best with respect to the hemisphere approach. The thickness of cluster 2 (HA subject) is not significantly high for CSF and GM, in the left hemisphere. This narrow silhouette is interpreted as a spread of the point inside the cluster and as a slightly inadequate separation of the cluster.

Table 4.14 Average silhouette width for evaluating clustering validity

Clasa	WB	LH	RH
H	0.9176	0.935	0.9284
HA	0.9829	0.9774	0.9326
IS	0.9989	0.8578	0.9296

The results of the correlation analysis, for each pair of classes, are presented in table 4.15. The results indicate that the HA and IS classes are not correlated, because the correlation coefficient is close to zero. This observation leads to the following hypothesis: H is the dependent variable and HA and IS are not correlated and are the independent variables

4.2.4 Gaussian mixture models (GMM) for brain DTI texture characterization

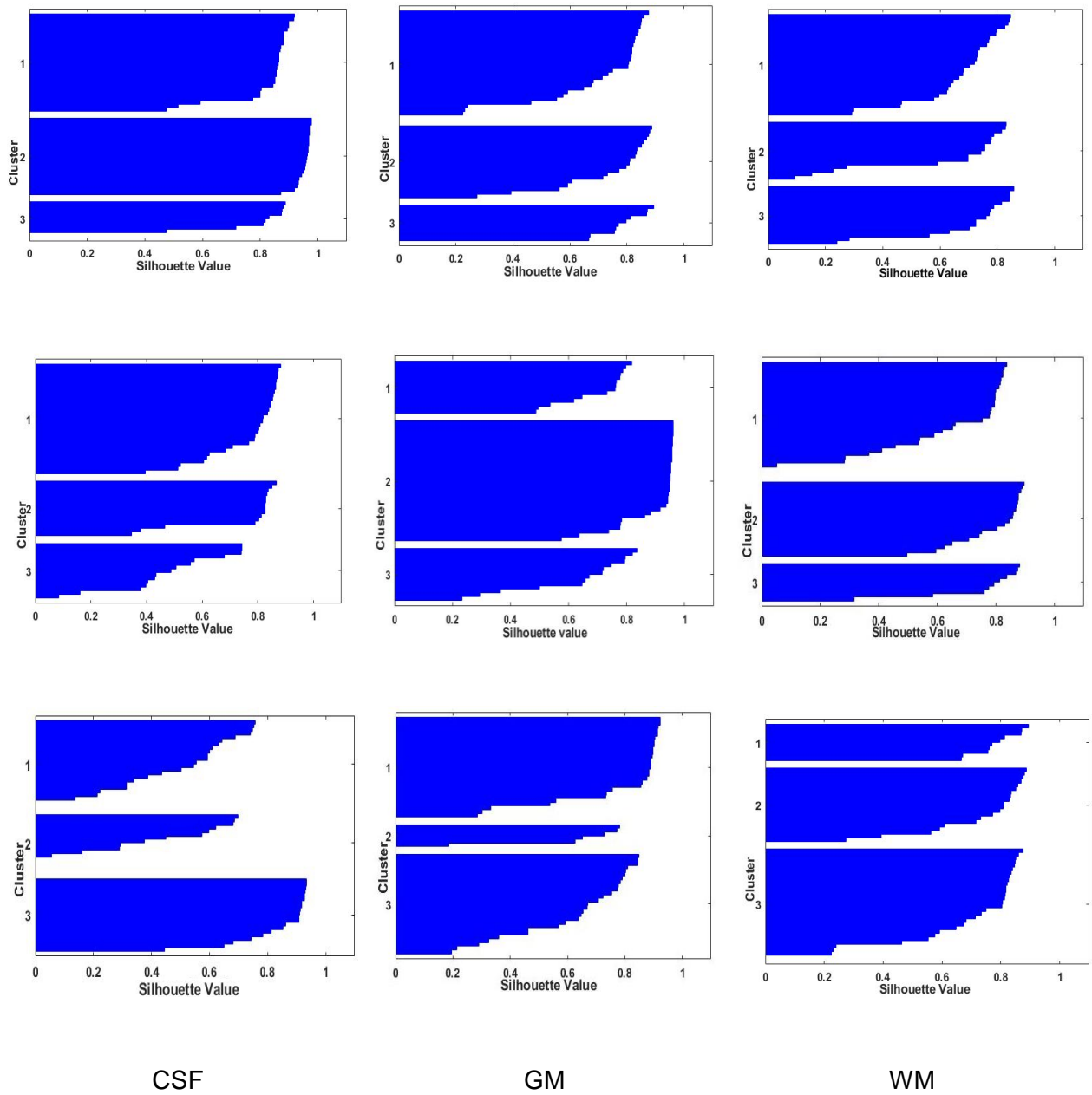


Figure 4.11 Silhouettes of a data set for three clusters (1 is for healthy subject, 2 for HA and 3 for IS)
Line 1: whole brain; Line 2: right hemisphere; Line 3: left hemisphere

Table 4.15 Correlation coefficients and multiple correlation coefficients.

	Correlation coefficient									Multiple correlation coefficient		
	$r_{HA,H}^1$	$r_{HA,H}^2$	$r_{HA,H}^3$	$r_{IS,H}^1$	$r_{IS,H}^2$	$r_{IS,H}^3$	$r_{IS,HA}^1$	$r_{IS,HA}^2$	$r_{IS,HA}^3$	$R_{H-(IS,HA)}^1$	$R_{H-(IS,HA)}^2$	$R_{H-(IS,HA)}^3$
LH	0.658	-0.421	0.214	0.654	0.515	-0.612	0.214	-0.031	0.295	0.528	0.429	0.545
RH	0.751	-0.773	0.654	0.443	0.339	0.622	0.336	-0.214	0.345	0.714	0.699	0.564

The results of this study were published in [37] Luminita Moraru, Simona Moldovanu, Lucian Traian Dimitrievici, Nilanjan Dey, Amira S. Ashour, Fuqian Shi, Simon James Fong, Salam Khang, Anjan Biswas, Gaussian mixture model for texture characterization with application to brain DTI images, Journal of Advanced Research 16 (2019) 15–23, <https://doi.org/10.1016/j.jare.2019.01.001>

4.2.6 Conclusions

-The study on the morphological asymmetry of brain tissues demonstrated the applicability of the method based on "histogram reduction" in differentiating brain disorders. The proposed method is fast and has low complexity, so it can be successfully used to efficiently process different brain MRI images.

-In the study of the characterization of brain structures from MRI images, we presented the possible use of the correlation function between the macroscopic and microscopic pixel arrangement by using entropy, as a local descriptor, and the FSIM and SSIM dissimilarity indices, as global descriptors, for different neurodegenerative diseases. It is found that for the neurodegenerative diseases studied, the most disordered distribution of the pixels was detected in the case of CCd brain calcification.

-The textural anisotropy of the brain structures specific to patients with Alzheimer's and Pick diseases and healthy subjects has been proposed as a tool capable of distinguishing between the two diseases. The proposed model is extremely sensitive because the area of imaging investigation has been reduced from the surface of the whole brain to the main cerebral lobes. The classification achieved had sensitivity > 90% and specificity > 80%. The development of a specific and sensitive anisotropic biomarker remains an active topic in future research.

Chapter V

Weighted diffusion imaging and tensor diffusion imaging

5.1 The apparent diffusion coefficient of water in brain tissues

Gray matter (GM), white matter (WM) and cerebrospinal fluid (CSF) for three different slices that were spaced at L = 79.8, 84.9 and 90 mm

The equation for diffusion-weighted imaging signal intensity is described by

$$S / S_0 = \exp(-b \cdot ADC) \quad (5.1)$$

where S / S_0 is the ratio of the signal with diffusion gradients(S) to signal without diffusion gradients, (S_0), $b[s/mm^2]$ is the attenuation factor and apparent diffusion coefficient that varies for CSF and non-CSF tissues.

The location of the ROIs cropped from different brain cellular structure in DW-MRI images is displayed in figure 5.1.

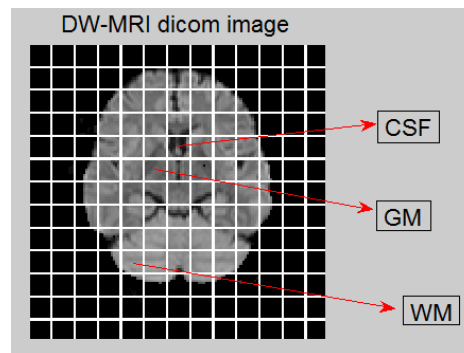


Figure 5.1 ROI's locations

Table 5.1 The averaged ADC values and standard deviation (SD) within each ROI for each slices

Slices	CSF			WM			GM		
	ADC (mm ² /s)	SD	e%	ADC (mm ² /s)	SD	e%	ADC (mm ² /s)	SD	e%
L1	2.01 E-03	1.87 E-04	4.1	6.12 E-04	1.16 E-04	6.1	6.97 E-04	1.14 E-04	2.3
L2	1.98 E-03	1.09 E-04	2.5	5.23 E-04	1.00 E-04	14.1	6.78 E-04	1.09 E-04	0
L3	1.82 E-03	1.73 E-04	5.6	6.55 E-04	1.11 E-04	6	6.67 E-04	1.33 E-04	2

In order to overcome the influence of the b-values and to obtain information regarding the structure of brain tissue, CSF and the membrane permeability in healthy human brain, the experimental data is achieved with the following b-values: $b_0=0$ s/mm²; $b_1=250$ s/mm²; $b_2=500$ s/mm²; $b_3=750$ s/mm²; $b_4=1000$ s/mm²; $b_5=1250$ s/mm².

The ROIs have been determined on the basis of different brain cellular structure. Their pixels appearance is presented in figure 5.2. The histographic characteristics of the brain ROIs in DW-MRI for tissues difference detection were used.

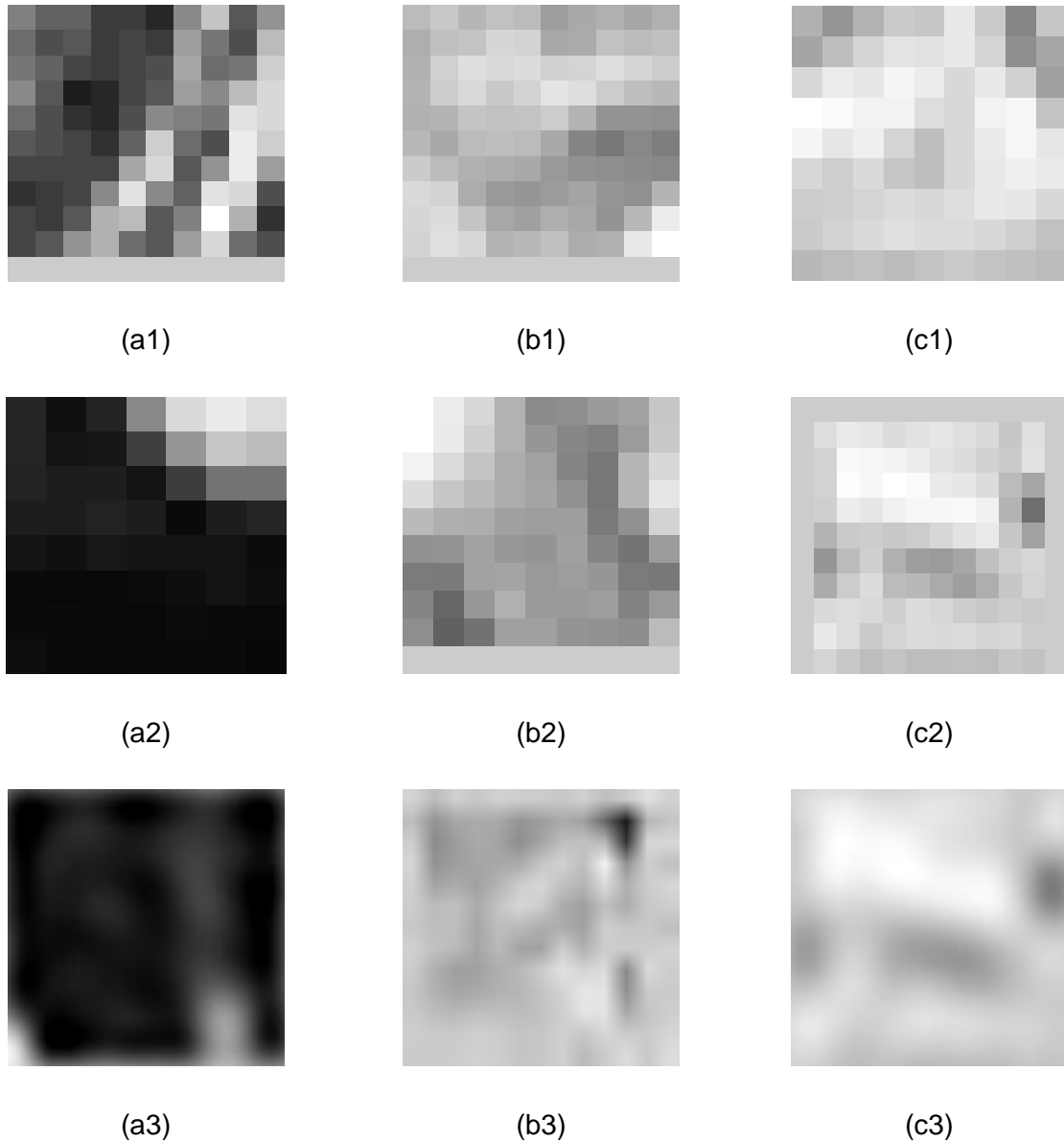


Figura 5.2 ROIs cropped from the targeted major brain structures. The first line is for L1 = 79.8 mm; the second line L2 = 84.9 mm; and the third line is for L3 = 90 mm. a) CSF; b) GM; c) WM

Weighted diffusion imaging and tensor diffusion imaging

By comparing the examined cerebral structures, the higher inter-site variation was obtained for WM and for the slice L2 = 84.9 mm. It is prone to the noise and edge effect of the anatomic structures (fig. 5.2, second line). For all b -value combinations a paired t-test has been performed and its results indicated that ADCs are significant for analyzed brain tissues and CSF with 95% confidence. For all ROIs, the mean ADC values were in the cortical gray matter, $(0.681 \pm 0.07) \cdot 10^{-3} \text{ mm}^2 / \text{s}$ (intervalul, $0.56\text{--}0.78 \cdot 10^{-3}$, in the white matter, $(0.613 \pm 0.10) \cdot 10^{-3} \text{ mm}^2 / \text{s}$ (intervalul $0.319\text{--}0.686 \cdot 10^{-3} \text{ mm}^2 / \text{s}$) and in CSF $(1.93 \pm 0.28) \cdot 10^{-3} \text{ mm}^2 / \text{s}$ (intervalul $1.59\text{--}2,43 \cdot 10^{-3} \text{ mm}^2 / \text{s}$).

Figure 5.3 illustrates one example for all analyzed cerebral structures.

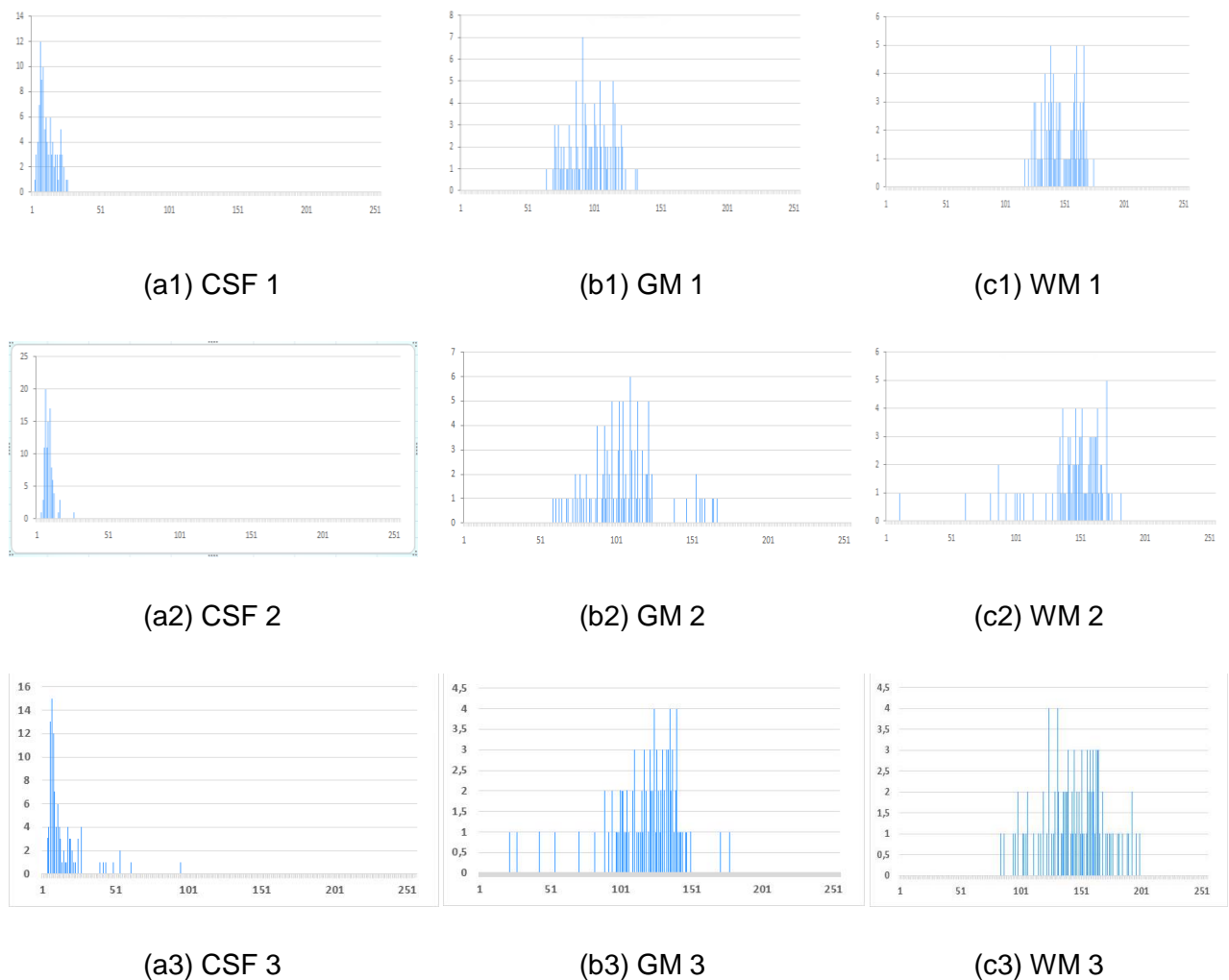


Figure 5.3 The histograms of the raw DW-MRI. The first line is for L1 = 79.8 mm; the second line L2 = 84.9 mm; and the third line is for L3 = 90 mm. a) CSF; b) GM; c) WM.

The signal dependencies - the attenuation factor b of the equation obtained for the three types of brain tissues are presented below:

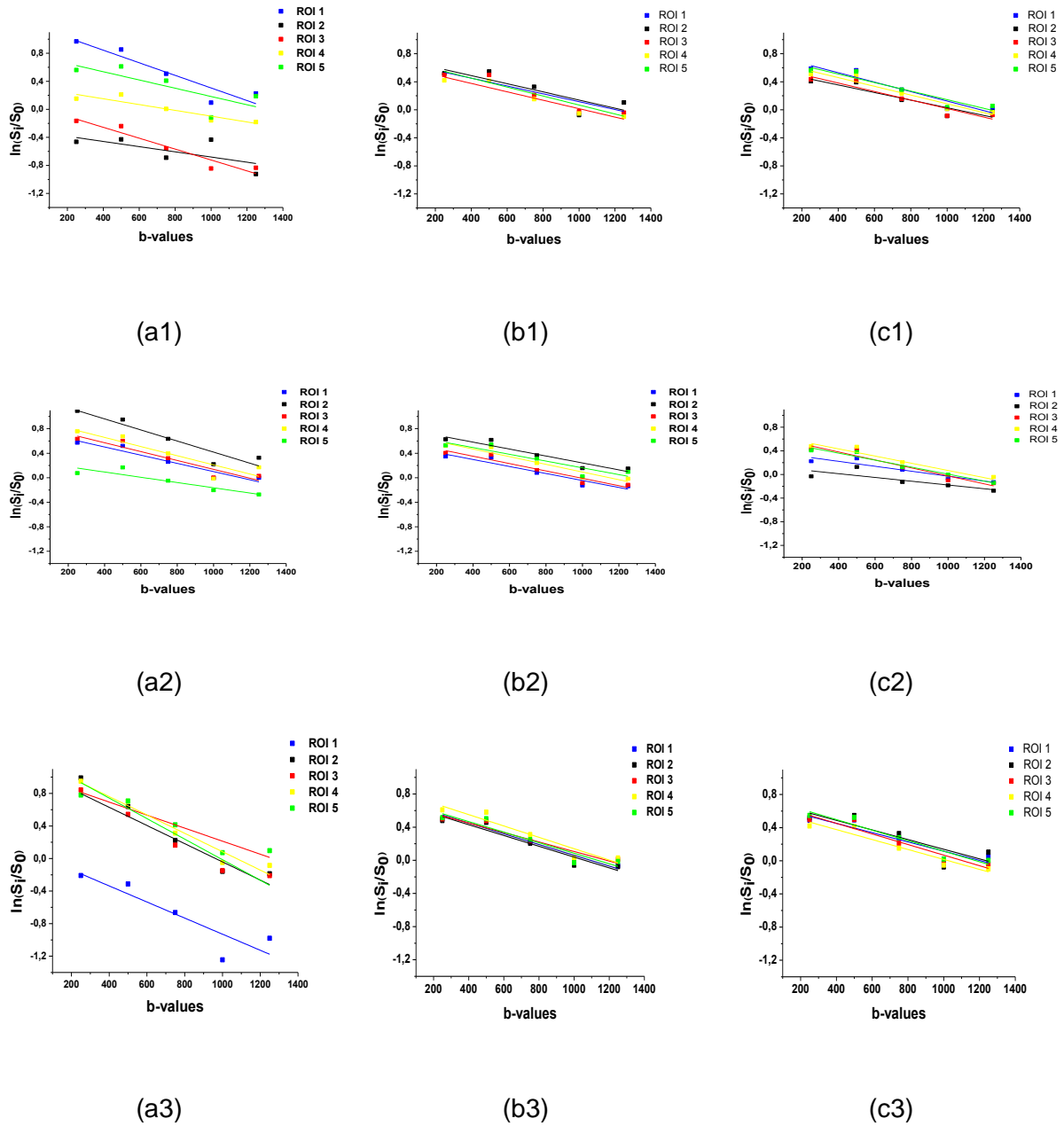


Figure 5.4 Signal-versus- b curves ($\ln(S/S_0) = f(b)$) over five brain ROIs. The first line is for $L1 = 79.8$ mm; the second line $L2 = 84.9$ mm; and the third line is for $L3 = 90$ mm. a) CSF; b) GM; c) WM.

Weighted diffusion imaging and tensor diffusion imaging

ADC values for a specific analyzed cerebral structure placed in the various location of the brain did not differ significantly. On the other hand, the mean cerebrospinal fluid ADC value was significantly higher than the mean white and gray matter values .

Figure 5.5 summarized the inter-site analysis and reproducibility of the apparent diffusion coefficient value..

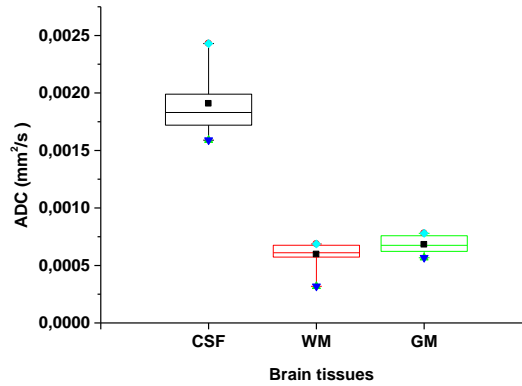


Figure 5.5 ADC values (mean \pm SD) averaged over small 10X10 ROIs in the cortical gray matter, in the white matter and into CSF for all b-value combinations.

5.2 Magnetic field gradients and their effects on the diffusion tensor derivate measures

This study aims to find the effect of strong magnetic gradient fields in FA and MD values and their bias and between affected and reference data using a hemisphere approach:

$$\Delta FA_{left} = \sqrt{\sum_i (FA_{left}^{ICH} - FA_{left}^H)^2} \quad \text{și} \quad \Delta FA_{right} = \sqrt{\sum_i (FA_{right}^{ICH} - FA_{right}^H)^2} \quad (5.3)$$

For a quick visualization of tissue differences, the histographic characteristics of the brain hemispheres in DTI images for various magnetic gradient fields were used.

Figure 5.6 shows The natural differences between the left and right hemispheres. The effect of the strong magnetic field is visible when a shift of the center of the distribution of the pixels to the median distribution of the grayscale [0, 255] appears. Also, for higher magnetic field gradients histograms are slightly narrow.

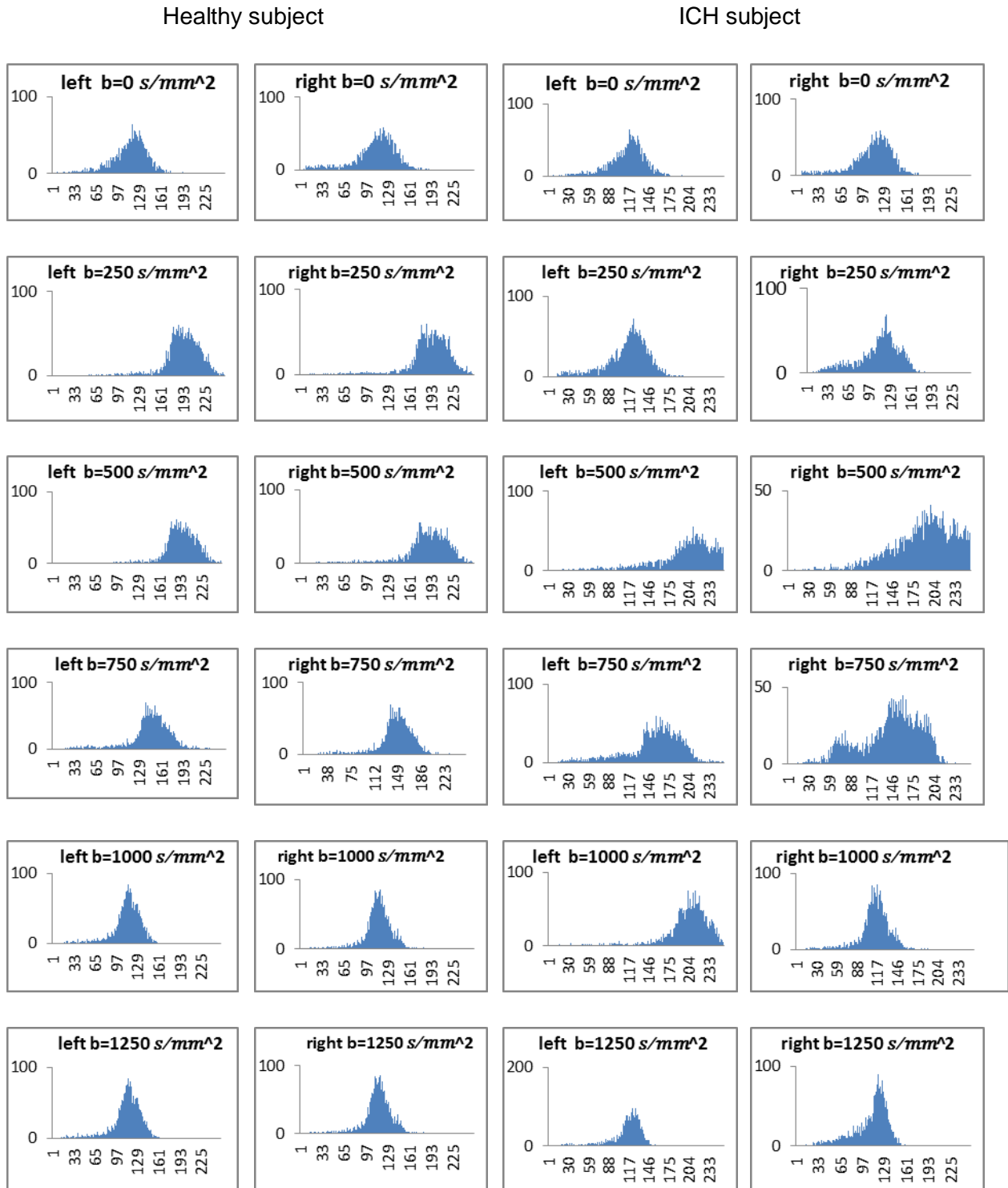


Figure 5.6 Examples of histograms of the left and right brain hemispheres for a healthy and ICH subject for different magnetic field gradients.

Weighted diffusion imaging and tensor diffusion imaging

The quantification of the bias in FA and MD difference between affected and reference data within a brain hemisphere approach is presented in figure 5.7.

For lower b-value combinations, ΔFA and ΔMD were significantly different between left and right hemispheres whereas for higher b-values these differences are minimized.

Comparison with reference data of healthy patients showed that higher gradients efficiently reduced bias in both FA and MD by reducing the artifacts.

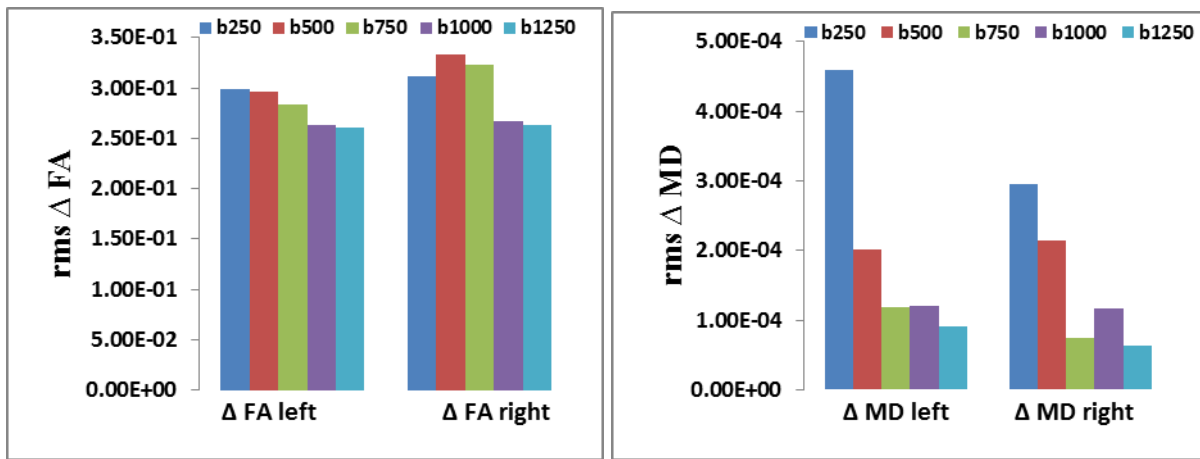


Figure 5.7 The bias in FA and MD by using the root-mean-square difference between subjects affected by ICH compared with healthy subjects, for various magnetic field gradients

5.3 The diffusion maps and the parameters associated with the diffusion tensor, in an analysis based on cerebral hemispheres.

5.3.1 Measures of diffusion anisotropy

-are described Trace $Tr(D)$ (1.7), Mean diffusivity, (MD) (1.3), the axial diffusivity D_{\parallel} (1.4) and radial diffusivity D_{\perp} (1.15).

5.3.2 Three-phase (3P) plot

The anisotropy shape measures, namely the linear-, planar-, and spherical anisotropy are defined respectively as follows:

$$c_L = \frac{\lambda_1 - \lambda_2}{3Tr(D)} \quad (5.3)$$

$$c_P = \frac{2(\lambda_2 - \lambda_3)}{3Tr(D)} \quad (5.4)$$

$$c_s = \frac{\lambda_3}{3Tr(D)} \tag{5.5}$$

5.3.3 Detectability index

The detectability index discriminates between the analyzed classes. It is based on the mean of the anisotropy values

$$d = \frac{\langle A_1 \rangle - \langle A_2 \rangle}{\sqrt{\sigma_1^2 + \sigma_2^2}} \tag{5.6}$$

Table 5.2 established a decrease in the FA (that may indicate myelin or axon membrane damages or a reduction of axonal packing density) and an increase in MD values for patients with brain injuries.

Table 5.2 Diffusion characteristics (mean SD) of the left and right hemispheres and of the whole brain across samples.

	H (N=3)			ICH (N=2)			IS (N=2)		
	LH	RH	WB	LH	RH	WB	LH	RH	WB
FA	0.204± 0.0208	0.205± 0.0359	0.205± 0.0572	0.196± 0.013	0.207± 0.0271	0.201± 0.0549	0.126± 0.0339	0.171± 0.0152	0.114± 0.0460
MD (mm ² /s ec)	(8.33± 0.72) 10 ⁻⁵	(7.21± 0.565) 10 ⁻⁵	(2.10± 0.93) 10 ⁻⁴	(1.24± 0.11) 10 ⁻⁴	(8.63± 0.58) 10 ⁻⁵	(2.51± 0.17) 10 ⁻⁴	(1.28± 0.01) 10 ⁻⁴	(8.17± 0.81) 10 ⁻⁵	(2.19± 0.11) 10 ⁻⁴
D (mm ² /sec)	(2.41± 0.13) 10 ⁻⁴	(2.06± 0.18) 10 ⁻⁴	(3.40± 0.14) 10 ⁻⁴	(1.91± 0.07) 10 ⁻⁴	(1.36± 0.49) 10 ⁻⁴	(2.22± 1.59) 10 ⁻⁴	(1.15± 0.57) 10 ⁻⁴	(0.75± 0.34) 10 ⁻⁴	(1.62± 0.72) 10 ⁻⁴
D _⊥ (m ² /sec)	(5.44± 1.61) 10 ⁻⁵	(6.12± 0.32) 10 ⁻⁵	(1.45± 0.71) 10 ⁻⁴	(9.05± 2.23) 10 ⁻⁵	(6.17± 1.26) 10 ⁻⁵	(1.66± 0.11) 10 ⁻⁴	(6.78± 2.32) 10 ⁻⁵	(7.70± 2.26) 10 ⁻⁵	(2.75± 0.44) 10 ⁻⁴

Typical images of the FA and *t*ADC tensor-metric maps for an example of the acquired sequences in healthy subjects as well as patients with ischemic stroke and temporal intracerebral haemorrhage are shown in the figure 5.8:

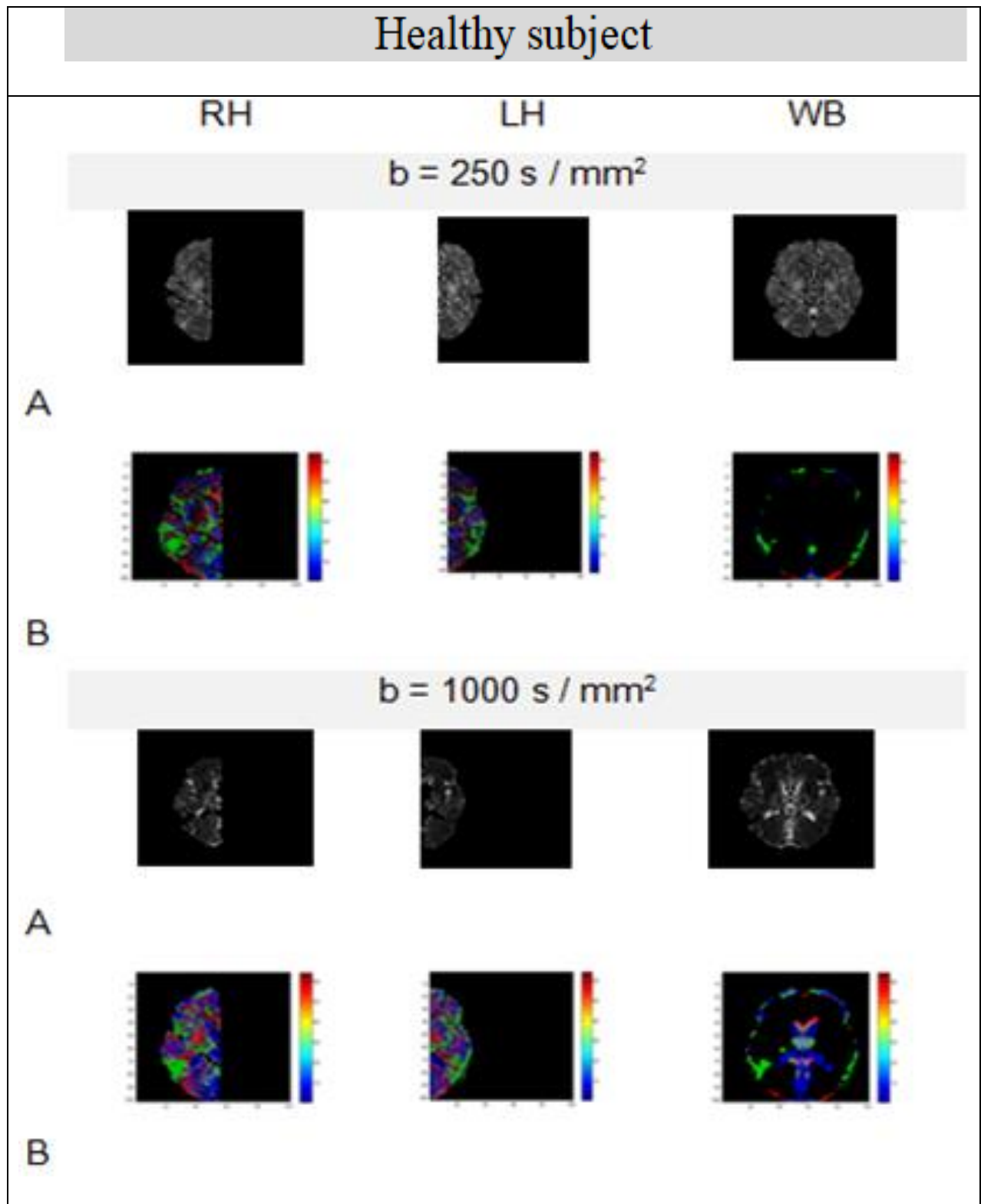


Figure 5.8 H Two levels of *diffusion weighting*, $b_1=250 \text{ s/mm}^2$ and $b_2=1000 \text{ s/mm}^2$ are presented. (A) FA tensor map - white areas indicate higher anisotropy; (B) tADC trace tensor map. Color code: red (left–right), green (anterior–posterior) and blue (superior–inferior).

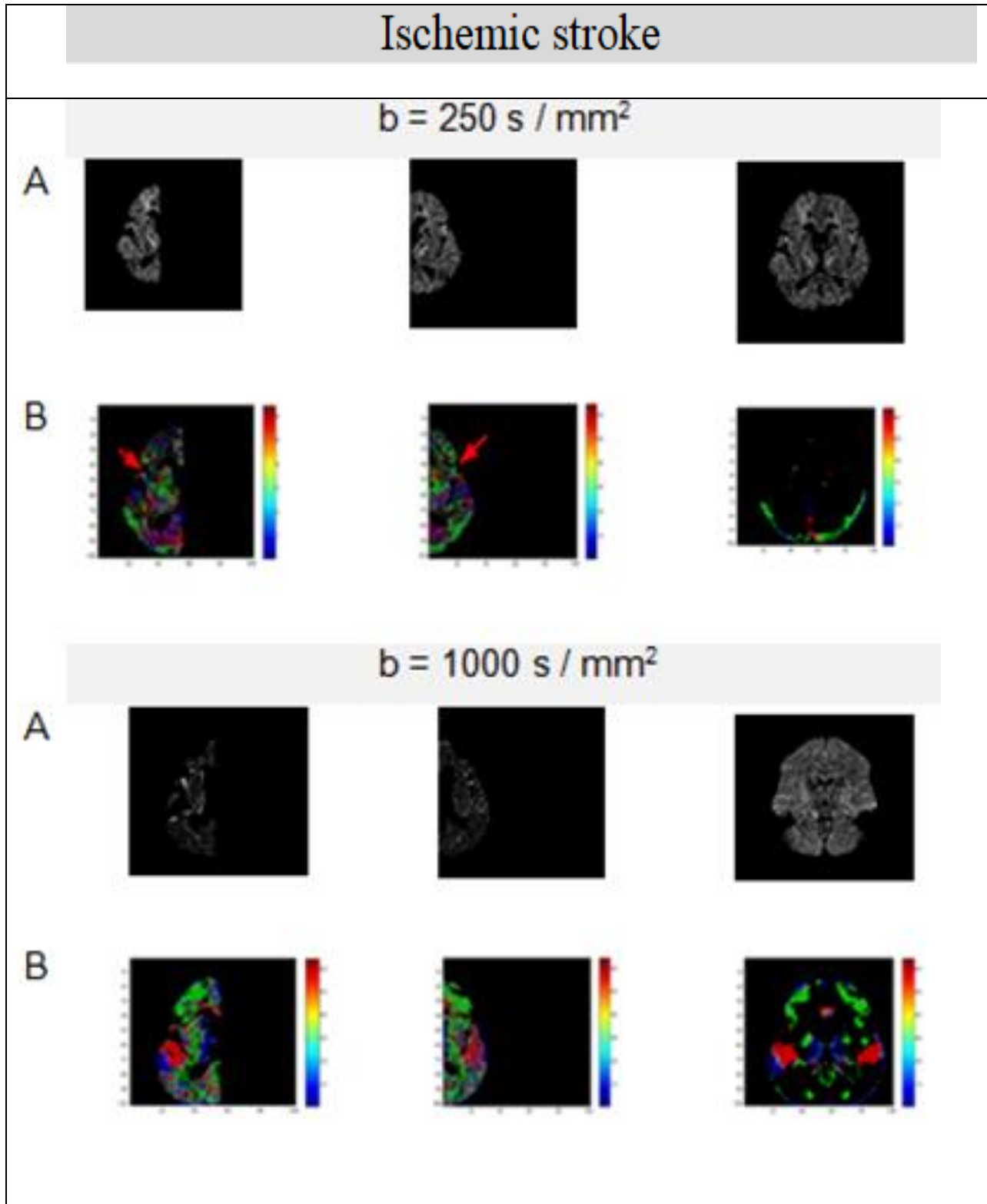


Figure 5.8 IS Two levels of *diffusion weighting* , $b_1=250 \text{ s/mm}^2$ and $b_2=1000 \text{ s/mm}^2$ are presented. (A) FA tensor map - white areas indicate higher anisotropy; (B) tADC trace tensor map. Color code: red (left–right), green (anterior–posterior) and blue (superior–inferior).

For IS images, tADC reveals decreased FA (diminished blue – red arrow). For ICH images (left temporal lobe – yellow arrow), tADC shows persistently decreased FA.

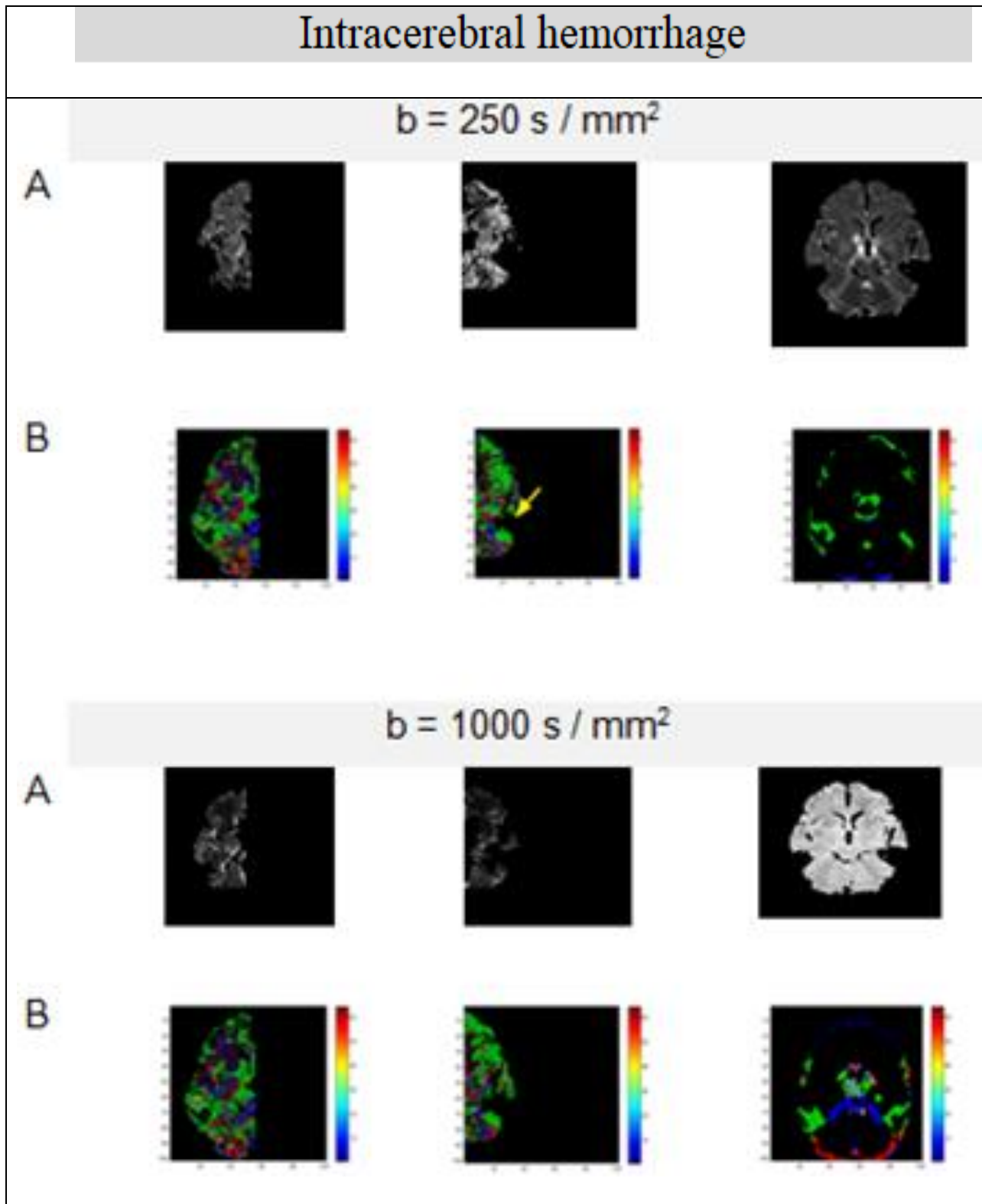


Figure 5.8 ICH Two levels of *diffusion weighting* $b_1=250$ s/mm² and $b_2=1000$ s/mm²

are presented. (A) FA tensor map - white areas indicate higher anisotropy; (B) tADC trace tensor map. Color code: red (left–right), green (anterior–posterior) and blue (superior–inferior).

The 3P plots that provide the trend in anisotropy with the change in the microstructural integrity of the brain are presented in Figure 5.9

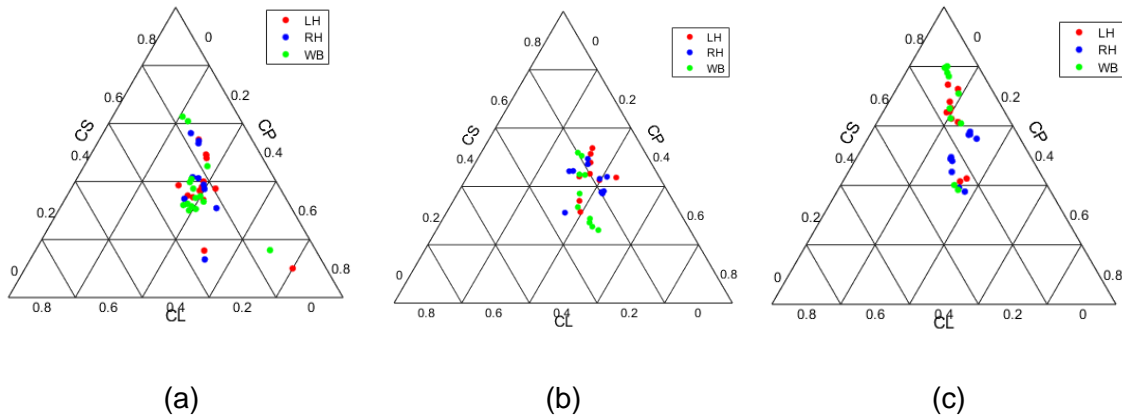


Figure 5.9

Three-phase plot for linear, planar and spherical measures of diffusion anisotropy for analyzed cases: (a) Healthy subjects, (b) ICH and (c) IS.

Figure 5.9 depicted that in the healthy subjects there is a similarity between the measured values of tensor shape for left and right hemispheres and a relative variation at the level of the entire brain. In addition, the ICH has an important contribution from the spherical anisotropy for LH and almost equal weights for RH, but a strong dissimilarity of anisotropy shape measures between brain hemispheres and entire brain are displayed. The IS has the higher spherical anisotropy behavior for the LH and whole brain, and almost equal weights of the linear and planar anisotropy for RH

Table 5.3 listed the estimated detectability results between left and right brain hemispheres and between each hemisphere and the entire brain, for each of the anisotropy measures.

Table 5.3 Detectability index d between left and right hemispheres for each anisotropy measure

	LH vs. RH			RH vs. WB			LH vs. WB		
	H	ICH	IS	H	ICH	IS	H	ICH	IS
FA	$5.99 \cdot 10^{-3}$	0.380	1.21	$6.92 \cdot 10^{-3}$	0.017	1.19	$1.18 \cdot 10^{-2}$	0.346	0.215
MD	0.011	0.302	0.315	1.17	0.915	0.992	1.08	0.631	0.543
D_{\parallel}	0.002	0.318	0.593	1.06	1.04	0.427	1.04	0.776	1.91
D_{\perp}	0.004	0.339	0.613	1.01	0.994	1.62	1.06	0.607	1.37

5.4 Measurement of non-Gaussian diffusion in brain tissues

It gives an inverse measure of the membrane density and according to data presented in Table 1, MD increases due to the degradation of the barriers to free water diffusivity in damaged tissues[39]. However, the MD has an opposite correlation to FA, where it is very sensitive to edema or necrosis.

The results of this study were published in [40] L. Moraru, S. Moldovanu, **L. T. Dimitrievici**, F. Shi, A. S. Ashour, N. Dey, *Quantitative Diffusion Tensor Magnetic Resonance Imaging Signal Characteristics in the Human Brain: A Hemispheres Analysis*, IEEE SENSORS JOURNAL, VOL. 17, NO. 15, AUGUST 1, 2017, pp 4886-4893

5.4 Measurement of non-Gaussian diffusion in brain tissues

5.4.1 Series expansion method

In the brain, diffusion is anisotropic as the measured value depends on the direction. Anisotropic diffusion is adequately represented by a symmetric effective (or apparent) diffusion tensor (i.e. it has six independent parameters):

$$\begin{aligned} \ln S(\mathbf{b}) &= \ln S(\mathbf{0}) - \mathbf{bD}_{app} + O(b^2) = \\ &= \ln S(\mathbf{0}) - \sum_{i=x,y,z} \sum_{j=x,y,z} b_{ij} D_{ij} + O(b^2) = \\ &= (-b_{xx} D_{xx} + 2b_{xy} D_{xy} + 2b_{xz} D_{xz} + b_{yy} D_{yy} + 2b_{yz} D_{yz} + b_{zz} D_{zz}) + O(b^2) \end{aligned} \quad (5.7)$$

Equation (5.7) becomes for non-Gaussian diffusion:

$$\ln S(\mathbf{b}) = \ln S(\mathbf{0}) - \mathbf{bD}_{app} + \frac{1}{6} b^2 D_{app}^2 K_{app} + O(b^3) \quad (5.8)$$

For b_1 , b_2 and b_3 , the diffusion D and kurtosis K coefficients are given by:

$$D \approx \frac{(b_3+b_2)D^{(12)} - (b_2+b_1)D^{(13)}}{b_3-b_2} \quad (5.9)$$

$$K \approx 6 \frac{D^{(12)} - D^{(13)}}{(b_3-b_2)D^2} \quad (5.10)$$

where $D^{(12)} \approx \frac{1}{b_2-b_1} \ln \frac{S(b_2)}{S(b_1)}$ and $D^{(13)} \approx \frac{1}{b_3-b_1} \ln \frac{S(b_3)}{S(b_1)}$ were estimated from DTI images..

The plots of diffusion-weighting dependence of the diffusion coefficient and diffusional kurtosis for CSF, GM and WM provided by Series expansion method are presented in figure 5.10. The linear dependencies plotted in the left column fit the equation (2) which describes the Gaussian diffusion and those plotted in the right column fit the equation (5) of non-Gaussian diffusion. The diffusion model has the kurtosis coefficient $K = 0$. In the case of DKI model, the logarithm of the signal intensity fits to a parabola.

The trend lines for both linear and polynomial dependencies are indicated for comparison purposes. Also the equation of the trend lines and the correlation coefficients are provided.

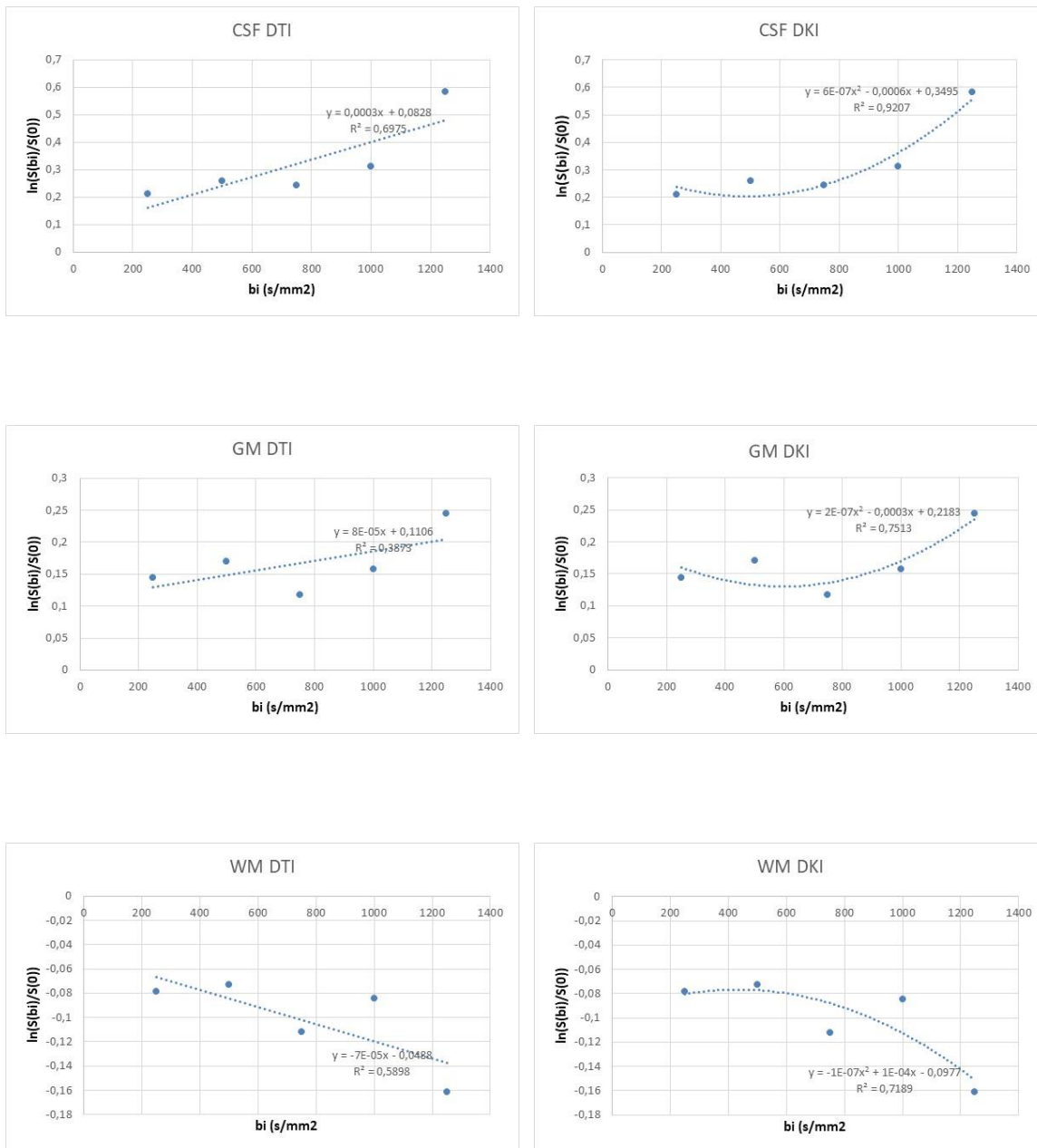


Figure 5.10 DTI and DKI models for brain tissues.

Table 5.4 Parameters of Gaussian and non-Gaussian diffusion models provided by Series expansion method (denoted as $\bar{\cdot}$) and by approximation method, for two normal healthy young adults

CSF					GM					WM				
\bar{D}	D	K	$\frac{1}{6} D^2 K$	$\frac{1}{6} D^2 K$	\bar{D}	D	K	$\frac{1}{6} D^2 K$	$\frac{1}{6} D^2 K$	\bar{D}	D	K	$\frac{1}{6} D^2 K$	$\frac{1}{6} D^2 K$
$3 \cdot 10^{-4}$	$0,77 \cdot 10^{-4}$	0.85	0.6	$8,56 \cdot 10^{-6}$	0.8	$0,22 \cdot 10^{-4}$	1.0	0.2	$3,74 \cdot 10^{-6}$	$0,7 \cdot 10^{-4}$	$0,113 \cdot 10^{-4}$	2.5	10^{-7}	$5,44 \cdot 10^{-7}$

According to the data in Table 5.4, some variations of diffusion and kurtosis coefficients are observed between the calculated and estimated values. The diffusion coefficient estimates

5.5 Conclusions:

are accurate to within about 25% for CSF, 27% for GM and 16% for WM. The diffusional kurtosis estimates are accurate to within about 15% for CSF, 28% for GM and 47% for WM.

5.5 Conclusions:

1) Analysis of the ADC coefficient values specific to the main brain tissues shows that the mean free water content of GM is higher than in WM. On the other hand, all WM structures have higher myelin water values than all GM structures; consequently, white matter shows hyperintensity relative to the gray matter. The ADC values in the CSF are almost two times higher than the gray and the white matter values because the water diffusion is much less restricted in the CSF than in the brain tissue.

2) We have shown that the effect of magnetic field gradients on the pixel distribution in diffusion tensor images and on diffusivity measures such as FA and MD. The results suggested, in the hemorrhage cases, the average FA values decreased. Our data are in agreement with the plethora of research studies that reported the reduction of FA in a case of various brain diseases. Also, MD increases and this could be correlated to the increase of tissue water content after intracerebral hemorrhage.

3) The main findings of the proposed analysis for the diffusion tensor and its parameters were:

(i) the hemisphere approach led to an improved estimation of the anisotropy measures. Hence, better assessment of the microstructural integrity of the brain was obtained when the hemorrhagic brain injuries were compared to the healthy subjects;

(ii) three-phase plot allows the visualization of the shape properties of anisotropy measures and this can speed up the comparison between different brain injuries

(iii) some anisotropy measures were more appropriate than others in discriminating between brain injuries. Thus, FA better separates healthy from ICH and IS - induced brain injury subjects, whereas the radial diffusivity better discriminates between the left and right hemispheres versus the whole brain for ICH and IS subjects. These results justify the proposed choice to use four measures of diffusion tensor anisotropy in the current analysis. For further improvement, the 3P maps were used to visualize the specific shape feature of the diffusion tensor.

General conclusions and future research

- A method has been proposed to search for the correlation between spatial pixel distribution and microstructure attributes of neurodegenerative diseases of Alzheimer's, Pick's and brain calcinosis, based on entropy, in an RGB approach.

-We developed a method to estimate the diffusion tensor shape for each hemisphere and for the entire brain based on linear, planar and spherical measures in a 3-phase plot in order to map and to compare the changes in anisotropy from healthy to hemorrhagic brain injury.

-We have proposed a predictive model that allows the association of a pathology with a certain area of the brain (frontal, parietal and temporal lobes) using the values of structural anisotropy. The main challenge in the proposed model is the minimization of the analyzed brain area, while still achieving a high classification rate. It is a merit of the proposed model to statistically distinguish between Alzheimer's and Pick's diseases when basically the same types of imaging data are required to develop this model.

-We have proposed a classification scheme based on Gaussian mixed models, GMM, to identify the variability of brain tissue in DTI images.

GMM has been shown to provide faster statistics with a high predictability rate

Future research directions pursued:

- The study of new methods of digital image processing with medical applications.

In this regard, the study of Matlab programming environments will be started, including the Image Processing and Python library, especially of the nipy, dipy, nibabel packages in order to develop a general structure of a brain image processing system.

- The effective calculation of the coefficients (W_{ijkl}) values that define the Kurtosis tensor, respectively of the other anisotropic sizes, such as the fractional anisotropy Kurtosis (KFA), the generalized fractional anisotropy (GFA), etc. from non-Gaussian diffusion.

Selective references

- [1] R. Brown, *A brief account of microscopic observations made on the particles contained in the pollen of plants*, London and Edinburgh Philosophical Magazine and Journal of Science, 4:161–173, 1828;
- [2] J. R. Alger, *The Diffusion Tensor Imaging Toolbox*, J Neurosci, 2012 May 30, 32(22): 7418–7428. doi:10.1523/JNEUROSCI.4687-11.2012;
- [5] M. Smoluchowski, *Zur kinetischen Theorie der Brownschen Molekulabewegung und der Suspensionen*, Annalen der Physik, 1906; 21:756–780;
- [4] K. R. Castleman, *Digital Image Processing*, Prentice Hall, Englewood Cliffs, NJ, (1996);
- [5] C. Vertan, M. Ciuc, *Tehnici Fundamentale de Prelucrarea și Analiza Imaginilor*, Editura MatrixROM, București, 2007;
- [6] C. Grava, V. Buzuloiu, *Elemente de prelucrarea și analiza imaginilor*, Editura Universității Oradea, 2007;
- [7] C. Vertan, *Prelucrarea și analiza imaginilor*, Editura Printech, București, 1999;
- [8] A. McAndrew, *An Introduction to Digital Image Processing with Matlab*, Publisher Course Technology, (2004);
- [9] S. Moldovanu, L. Moraru, A. Biswas, *Robust skull stripping segmentation based on irrational mask for magnetic resonance brain images*, J Digit Imaging 29(6):738–747, 2015;
- [10] D. Adam, S. Beilin-Nissan, Z. Friedman, V. Behar, *The combined effect of spatial compounding and nonlinear filtering on the speckle reduction in ultrasound images*, Ultrasonics, Vol. 44, pp. 166–81, 2006;
- [11] M. Ivanovici, *Procesarea Imaginilor - Îndrumar de laborator*, Editura Universității Transilvania, Brașov, 2006;
- [12] M. C. Motwani, M. C. Gadiya, R.C. Motwani, *Survey of Image Denoising Techniques*, Proceedings of GSPx, Santa Clara, CA, 2004;
- [13] E. Arias-Castro, D. L. Donoho, *Does median filtering truly preserve edges better than linear filtering?*, Annals of Statistics, Vol. 37(3), pp. 1172–1206, 2009;
- [14] P. Hellier, C. Barillot, I. Corouge, B. Gibaud, G. Le Goualher, D.L. Collins, A.E.G. Malandain, N. Ayache, G.E. Christensen, H.J Johnson, *Retrospective evaluation of intersubject brain registration*, IEEE Trans Med Imaging, 22(9):1120-1130, 2003;
- [15] Filtering and Enhancing Images, <https://courses.cs.washington.edu/courses/cse576/book/ch5.pdf>, University of Washington, accesat aprilie 2019;
- [16] D. Cobzas, N. Birkbeck, M. Schmidt, M. Jagersand, A. Murtha, *3D Variational Brain Tumor Segmentation using a High Dimensional Feature Set*, International Conference on Computer Vision ICCV (2007), Rio de Janeiro, Brazil, 2007;
- [17] C. Buchel, T. Raedler, M. Sommer, M. Sach, C. Weiller, M. Koch, *White matter asymmetry in the human brain: a diffusion tensor MRI study*, Cerebral Cortex 14(9):945, 2004;

- [18] W. Zhou, A.C. Bovik, H. R. Sheikh, E. P. Simoncelli, *Image quality assessment: from error visibility to structural similarity*, IEEE T. Image Proc. Vol 13, No. 4, pp. 600-612, 2004;
- [19] M. R. Sabuncu, *Entropy-based Image Registration, thesis dissertation*, Princeton University Department of Electrical Engineering, New Jersey, United States, (2006);
- [20] L. Robin, *The entropic brain*, Revisited, March 2018, Neuropharmacology 142, DOI:10.1016/j.neuropharm.2018.03.010;
- [21] **L. T. Dimitrievici**, S. Moldovanu, L. Moraru, *Entropic characterization of random cerebral structures in MR images*, System Theory, Control and Computing (ICSTCC), 20th International Conference on Sinaia, 13-15 Oct. 2016, DOI: 10.1109/ICSTCC.2016.7790720, 2016;
- [22] e-Anatomy atlas at: <http://www.imaios.com/en>;
- [23] R.M. Haralick, *Statistical and Structural Approaches to Texture*, Proceedings of the IEEE, Vol. 67, pp. 786-804, <http://citeseerx.ist.psu.edu/viewdoc/download?doi=10.1.1.450.5220&rep=rep1&type=pdf>, (1979);
- [24] R. M. Neupaaauer, K. L. Powell, *A fully-anisotropic Morlet Wavelet to Identify Dominant Orientation in a Porous Medium*, Computer and Geosciences, Vol. 31, pp. 465-471;
- [25] R. M. Haralick, *Statistical and structural approaches to texture*, Proc IEEE 67:786–804, 1979;
- [26] P. S. Addison, *Wavelet transforms and the ECG: a review*, IOP Publishing LTD, Physiological Measurement, Volume 26, Number 5, 2005;
- [27] L. Piffet, *A locally anisotropic model for image texture extraction*, Mathematical Image Processing Springer Proceedings in Mathematics, Vol. 5, pp. 141-158, (2011);
- [28] Y. I. Zhu, X. Wu, I. L. Chern, *Derivative securities and difference methods*, Springer, New York, USA, Second Edition, pp. 29, ISBN 978-1-4614-7306-0, 2013;
- [29] L. Saba, N. Dey, A. S. Ashour, S. Samanta, S. S. Nath, S. Chakraborty, J. Sanches, D. Kumar, R. T. Marinho, J. S. Suri, *Automated stratification of liver disease in ultrasound: an online accurate feature classification paradigm*, Comput Methods Programs Biomed 130:118–134, 2016;
- [30] L. Moraru, S. Moldovanu, **L. T. Dimitrievici**, N. Dey, A. S. Ashour, *Texture Anisotropy technique in Brain Degenerative Diseases*, Neural Computing and Applications, Volume 30, Issue 5, 1 September 2018, Pages 1667-1677 DOI 10.1007/s00521-016-2777, 2018;
- [31] J. Wang, *Discriminative Gaussian mixtures for interactive image segmentation*. In: Proceeding of the IEEE International Conference on Acoustics, Speech and Signal Processing (ICASSP); 2007; 386–96;
- [32] G. McLachlan, D. Peel, *Finite mixture models*: Wiley series in probability and mathematical statistics. Wiley. (NY), 2000;
- [33] J. R. Hershey, P. A. Olsen, *Approximating the Kullback Leibler divergence between Gaussian mixture models*, In: IEEE International Conference on Acoustics, Speech and Signal Processing 2007; 4: 317-320;

Selective references

- [34] J. Cohen, *Statistical Power Analysis for the Behavioral Sciences*. Second Edition, Lawrence Erlbaum Associates, USA; 1988;
- [35] K. E. Watkins, T. Paus, J. P. Lerch, A. Zijdenbos, D. L. Collins, P. Neelin, et al. *Structural asymmetries in the human brain: a voxel-based statistical analysis of 142 MRI scans*. *Cereb Cortex* 2001; 11(9): 868-77;
- [36] G. Gong, T. Jiang, C. Zhu, Y. Zang, F. Wang, S. Xie et al, *Asymmetry analysis of cingulum based on scale-invariant parameterization by diffusion tensor imaging*. *Hum Brain Mapp* 2005; 24(2): 92–98;
- [37] L. Moraru, S. Moldovanu, **L. T. Dimitrievici**, N. Dey, A. S. Ashour, F. Shi, S.J. Fong, S. Khan, A. Biswas, *Gaussian mixture model for texture characterization with application to brain DTI images*, *Journal of Advanced Research* 16, <https://doi.org/10.1016/j.jare.2019.01.001>, 2019;
- [38] D. Le Bihan, E. Breton, D. Lallemand, P. Grenier, E. Cabanis, M. R. Laval-Jeantet, *MR imaging of intravoxel incoherent motions: application to diffusion and perfusion in neurologic disorders*, *Radiology*. 161:401–407. [PubMed: 3763909], 1986;
- [39] G. P. Winston, *The physical and biological basis of quantitative parameters derived from diffusion MRI*, *Quant Imaging Med Surg.*, vol. 2, no.4, pp. 254–265, 2012;
- [40] L. Moraru, S. Moldovanu, **L. T. Dimitrievici**, F. Shi, A. S. Ashour, N. Dey, *Quantitative Diffusion Tensor Magnetic Resonance Imaging Signal Characteristics in the Human Brain: A Hemispheres Analysis*, *IEEE SENSORS JOURNAL*, VOL. 17, NO. 15, AUGUST 1, 2017, pp 4886-4893;
- [41] C. M. W. Tax, W. M. Otte, M. A. Viergever, R. M. Dijkhuizen, A. Leemans (2014), *REKINDLE: Robust extraction of kurtosis INDices with linear estimation*, *Magnetic Resonance in Medicine* 73(2): 794-808;
- [42] S. Pajevic, C. Pierpaoli, *Color schemes to represent the orientation of anisotropic tissues from diffusion tensor data: application to white matter fiber tract mapping in the human brain*, *Magn Reson Med*.2000; 43:921. [PubMed: 10861892];
- [43] S. Annadurai, R. Shanmugalakshmi, *Fundamentals of digital image processing*, Pearson Education, Dorling Kindersley (India) Pvt. Ltd., 2007;
- [44] S.K. Narayanan, R.S.D. Wahidabanu, *A View on Despeckling in Ultrasound Imaging*, *Image Processing and Pattern Recognition* 2(3):85-98, 2009;
- [45] L. Moraru, **L. T. Dimitrievici**, V. A. Moraru, *Structural brain asymmetry evaluated by histogram analysis and similarity metrics*, *Annals of “Dunarea De Jos” University Of Galati Mathematics, Physics, Theoretical Mechanics Fascicle II*, Year , Year VIII (XXXIX), No. 1, pp 13-19, 2016;

Research results

Articles published in ISI journals

1. L. Moraru, S. Moldovanu, **L. T. Dimitrievici**, N. Dey, A. S. Ashour, F. Shi, S. J. Fong, S. Khang, A. Biswas, Gaussian mixture model for texture characterization with application to brain DTI images, Journal of Advanced Research, Volume 16 (2019), Pages 15–23, doi:10.1016/j.jare.2019.01.001, 2019, IF 4.327; zona rosie
2. L. Moraru, S. Moldovanu, **L. T. Dimitrievici**, N. Dey, A. S. Ashour, Texture Anisotropy technique in Brain Degenerative Diseases, Neural Computing and Applications, Volume 30, Issue 5, pp1667-1677, 2018, doi: 10.1007/s00521-016-2777-7, IF 4.213; zona rosie
3. L. Moraru, S. Moldovanu, **L. T. Dimitrievici**, F. Shi, A. S. Ashour, N. Dey, Quantitative Diffusion Tensor Magnetic Resonance Imaging Signal Characteristics in the Human Brain: A Hemispheres Analysis, IEEE SENSORS JOURNAL, Volume 17, Issue 15, pp 4886-4893, doi: 10.1109/JSEN 2017-2714701, 2017, IF 2,512, zona galbena.

Articles published in ISI indexed volumes

1. L. Moraru, **L. Dimitrievici**, Apparent diffusion coefficient of the normal human brain for various experimental conditions, American Institute of Physics AIP Conf. Proc. 1796 (2017), TIM15-16 Physics Conference, pp 040005-1–040005-6; doi: 10.1063/1.4972383, ISBN: 978-0-7354-1462-4;
2. L. Moraru, **L. T. Dimitrievici**, A. Ene, S. Moldovanu, *Magnetic field gradients and their effects on the diffusion tensor derivate measures*, DOI: 10.21175.42 RadProc.2017.42, RAD Conference Proceedings, ISSN 2466-4626 (on line), vol2, Pages: 207-211, 2017
3. **L. T. Dimitrievici**, S. Moldovanu, L. Moraru, Entropic characterization of random cerebral structures in MR images, IEEE Xplore, pages 532-536, 19 dec 2016, doi: 10.1109/ICSTCC.2016.7790720; System Theory, Control and Computing (ICSTCC), 2016 20th International Conference on, Date of Conference: 13-15 Oct. 2016, Sinaia

Articles published in BDI journals

1. L. Moraru, **L. Dimitrievici**, V. A. Moraru, Structural brain asymmetry evaluated by histogram analysis and similarity metrics, Annals of “Dunarea De Jos” University of Galati Mathematics, Physics, Theoretical Mechanics Fascicle II, Year VIII (XXXIX), 2016, No. 1, pp 13-19;
2. L. Moraru, **L. Dimitrievici**, The non-Gaussian diffusion quantification of brain tissues, Annals Of “Dunarea De Jos” University of Galati, Mathematics, Physics, Theoretical Mechanics, Fascicle II, Year IX (XL) 2017, No. 1, pp 12-18
3. **L. T. Dimitrievici**, S. Moldovanu, L. Moraru, First order statistics-based features selection for clustering using Gaussian Mixture Model, Annals Of “Dunarea De Jos” University of Galati Mathematics, Physics, Theoretical Mechanics, Fascicle II, Year X (XLI), 2018, pp104-111;

Articles communicated at national and international conferences

1. **L. T. Dimitrievici**, S. Moldovanu, L. Moraru, Entropie characterization of random cerebral structures in MR images, System Theory, Control and Computing (ICSTCC), 20th International Conference on Sinaia, 13-15 Oct. 2016
2. L. Moraru and **L. Dimitrievici**, Apparent diffusion coefficient of the normal human brain for various experimental conditions, TIM 15-16 International Physics Conference West University of Timisoara 26th-28th of May, 2016
3. L. Moraru, **L. Dimitrievici**, A. Ene, S. Moldovanu, Magnetic field gradients and their effects on the diffusion tensor derivative measures, 5th International Conference on Radiation and Applications in Various Fields of Research, 12th-16th of June, Budva, Montenegro
4. L. Moraru, **L. Dimitrievici**, V. A. Moraru, Structural brain asymmetry evaluated by histogram analysis and similarity metrics, Scientific Conference of Doctoral Schools from UDJ Galati, CSSD-UDJG 2016, 4th Edition, 2th-3th of June 2016, Galati, Romania, <http://www.cssd-udjg.ugal.ro/index.php/registration>
5. L. Moraru, **L. Dimitrievici**, The non-Gaussian diffusion quantification of brain tissues, Scientific Conference of Doctoral Schools from UDJ Galati, CSSD-UDJG 2017, 5th Edition, 8th-9th of June 2017, Galati, Romania, <http://www.cssd-udjg.ugal.ro/index.php/registration>
6. **L. T. Dimitrievici**, S. Moldovanu, L. Moraru, First order statistics-based features selection for clustering using Gaussian Mixture Model, Scientific Conference of Doctoral Schools from UDJ Galati, CSSD-UDJG 2018, 6th Edition, 7th-8th of June 2018, Galati, Romania, <http://www.cssd-udjg.ugal.ro/index.php/registration>